Deciphering Faujasite Zeolite Dealumination at the Atomic Scale

Zhuoran Wang, Thomas Jarrin, Mickaël Rivallan, Isabelle Clémençon, Emmanuel Soyer, Theodorus de Bruin, Laurent Lemaitre, Virgile Rouchon, David Gajan, Gerhard Pirngruber, et al.

Zhuoran Wang, Thomas Jarrin, Mickaël Rivallan, Isabelle Clémençon, Emmanuel Soyer, et al.. Deciphering Faujasite Zeolite Dealumination at the Atomic Scale. ACS Catalysis, 2024, 14 (24), pp.18442-18456. 10.1021/acscatal.4c03036 . hal-04906958

Deciphering Faujasite Zeolite Dealumination at the Atomic Scale

Zhuoran Wang,[†‡*] Thomas Jarrin,[‡] Mickaël Rivallan,[‡] Isabelle Clémençon,[‡] Emmanuel Soyer,[‡] Theodorus de Bruin,[ǀ] Laurent Lemaitre,[‡] Virgile Rouchon,[‡] David Gajan,[†] Gerhard Pirngruber,[‡*] Céline Chizallet,[‡*] Anne Lesage[†*]

[†] Centre de RMN à Très Hauts Champs, Université de Lyon (CNRS/ENS Lyon/UCB Lyon 1), 69100 Villeurbanne, France

[‡] IFP Energies nouvelles, Rond-point de l'échangeur de Solaize, BP3, 69360 Solaize, France

[ǀ] IFP Energies nouvelles, 1 et 4 Avenue de Bois Préau, 92852 Rueil-Malmaison, France

KEYWORDS: zeolites; dealumination; solid-state NMR; DFT calculations; IR spectroscopy; quantitative analysis

ABSTRACT: Zeolites are widely used as solid acid catalysts from the laboratory to the industrial scale. Their thermal stability, mesoporous volume and catalytic properties can be significantly enhanced by framework dealumination, resulting in the formation of framework defects and extra-framework aluminum (EFAL) species, altering surface acidity and microporous volume. Understanding dealumination of as-synthesized zeolite crystals is critical to tune their catalytic activities. However, the atomic-scale structural evolution of the zeolite surface in the course of dealumination treatments remains elusive. Here, we examined a series of four faujasite zeolite samples, ranging from Y to USY zeolites, collected at key steps of the manufacturing process. High-resolution quantitative ^{1}H NMR spectra were obtained at high-field and fast magic angle spinning frequency and interpreted with the help of ^{1}H multiple-quantum (up to four-quanta) and ^{1}H-^{27}Al dipolar-based correlation experiments. An extensive array of surface species was resolved, identified, and monitored during dealumination with a high level of structural detail. This was achieved through a joint interpretation of the NMR data acquired across the entire sample set and DFT calculations spanning an exceptionally broad range of environments. Key insight is provided into the environment of various hydroxyl groups as well as the atomic-scale structure of mononuclear EFAL species. While alumina-like domains are not observed, the presence of multinuclear EFAL species is evidenced. The structure of several defect silanol sites were also characterized. The quantitative evolution of these various surface sites during dealumination is discussed based on the peak intensity changes in the ^{1}H spectra. Ultimately, in situ IR spectra were obtained. Clear correlations were observed between IR bands and ^{1}H chemical shifts, offering valuable perspectives to refine the interpretation of both IR and NMR spectra.

1. INTRODUCTION

Zeolites are microporous crystalline materials with structures built from corner-sharing AlO_4 and SiO_4 (or PO_4) tetrahedrons and extensively employed as heterogeneous catalysts in various industrial applications due to their unique chemical and physical properties, including stability, shape selectivity and tunable acidity.[1–6] The presence of Al atoms in the framework requires charge compensation by either extra-framework cations or protons covalently bound to the bridging O between Si and Al. These bridging hydroxyl groups generate the Brønsted acidity of zeolites. However, the ultimate acidic properties of zeolites are much more complex, as the final products typically undergo a series of (hydro)thermal and chemical treatments aimed at enhancing the stability and porosity of the pristine material.

An example is the transformation of the as-synthesized faujasite (FAU structure type) zeolite NaY into the ultrastable Y (USY) zeolite, a long-standing pivotal catalyst in refining and petrochemical industry used for fluid catalytic cracking, hydrocracking, alkylation or isomerization reactions.[6–12] Y zeolites also hold recent promise in biomass conversion[13–15] or plastic recycling.[16,17] Their crystal structures are constructed with supercages and sodalite cages interconnected through hexagonal prisms. The USY zeolites are typically prepared by a series of hydrothermal treatments, first conducted on partially NH_4^+-exchanged NaY zeolites (Figure 1). Steaming steps lead to the hydrolysis of Si-(OH)-Al bonds, displacing Al atoms from the framework, in what is known as the dealumination.[2,18,19] The generation of extra-framework aluminum (EFAL) species along with other framework-connected defect sites results in Lewis acidic sites, simultaneously modifying the vicinity and thus the acidity of Brønsted sites. A following leaching step using strong acid removes all or part of the EFAL species. These treatments lead to the formation of mesopores, whose acid sites have a different reactivity than those located in the micropores.[20] The resulting USY zeolite shows not only high thermal stability but also improved catalytic activity.

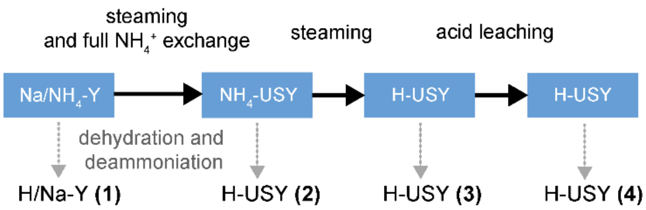

Figure 1. Schematic representation of industrial dealumination treatments applied to Y zeolites, and the series of four samples investigated here. Prior to analysis, the materials were activated as described in the experimental section, removing water and ammonium ions from the framework.

While these manufacturing protocols are widely employed in industry, a thoroughly fundamental understanding of dealumination mechanisms is still missing. Thus, the causal link between the industrial post-synthesis treatments and the atomic-scale transformation of the zeolite surface structure at each step of these manufacturing processes remains still elusive. Such knowledge, however, is essential for controlling dealumination and in turn designing zeolite materials with enhanced and tunable catalytic properties.

Solid-state nuclear magnetic resonance (NMR) spectroscopy, often in conjunction with powder X-ray diffraction (PXRD), Fourier transform infrared (FTIR) spectroscopy, elemental analysis, adsorption isotherm measurement and/or electron microscopy, has proven to be a versatile and insightful technique to investigate hydroxyl groups and monitor dealumination in zeolites.[21,22,31–35,23–30] Analyses are typically conducted after dealumination, as the conditions of treatments in terms of water vapor pressure and temperature do not permit *in situ* approaches, with the exception of PXRD.[36] Brønsted and Lewis acid sites are conventionally explored by one- (1D) and two-dimensional (2D) ^{1}H and ^{27}Al Magic Angle Spinning (MAS) NMR.[22–24,30,37–40] Distinct ^{27}Al NMR parameters are extracted for four-coordinated framework aluminum atoms associated with Brønsted acid sites and for five- or six-coordinated aluminum atoms usually assigned to Lewis acid sites.[39,41,42] Similarly, distinct ^{1}H chemical shifts are observed for Brønsted acid sites, EFAL species and framework or external surface defects. Various NMR strategies were implemented to determine the number of hydroxyl groups present in a given structural motif or spatial proximities between acid sites.[43–47] NMR spectroscopy of probe molecules with different sizes and base strengths were also implemented to monitor the relative acid strength of dealuminated zeolites and investigate vicinal acid pairs.[22,25,48,49]

While NMR can go a long way in characterizing the local structure of acid sites, a coupling with computational models is often necessary. Several density functional theory (DFT) models were developed to unravel the framework and surface structures of dealuminated zeolites, the distribution and nature of EFAL species, as well as the dealumination mechanisms.[6,19,50–55] By combining DFT calculations with ^{1}H NMR spectroscopy, several EFAL species, such as $Al(OH)_3$, $[Al(OH)]^+$ and $[Al(OH)_3(H_2O)_3]$, were proposed in dealuminated HY zeolite,[56,57] and silanol nests were evidenced in calcined zeolite SSZ-70.[47]

However, despite substantial research efforts, obtaining a comprehensive description of the evolution of zeolite surface structure in the course of dealumination remains an unmet challenge due to the considerable diversity of surface sites potentially formed during the processing of as-synthesized zeolites. Furthermore, many of the aforementioned studies were conducted on samples that do not represent industrial standards.

In this work, we investigate a series of four FAU zeolite samples, ranging from Y to USY zeolites collected at key steps of industrial dealumination treatments (Figure 1). By conducting NMR experiments at high field and fast MAS, we show that high resolution quantitative 1D ^{1}H NMR spectra are obtained that can be fully interpreted with the help of 2D ^{1}H multiple-quantum single-quantum (MQ-SQ) correlation experiments (up to four-quanta), as well as ^{1}H{^{27}Al} dipolar-based heteronuclear multiple quantum correlation (D-HMQC) experiments. An extensive set of individual proton resonances was resolved that could be assigned with a great level of structural details by a combined interpretation of the ensemble of NMR data acquired across the whole set of samples and DFT calculations encompassing an unprecedented large variety of environments. Subsequently, a quantitative analysis of the evolution of various species during dealumination is performed, providing novel insights into the structural changes of FAU zeolites during steaming and acid-leaching treatments. These results are further used to revisit the assignment of the IR spectra collected on the same set of FAU samples.

2. MATERIALS AND METHODS

2.1. Sample Preparation

Four commercial Y zeolites representing different stages in the dealumination process were purchased from Zeolyst (commercial codes CBV300, CBV500, CBV600 and CBV712). The samples were dehydrated (or activated) at 450 °C under high vacuum ($<10^{-5}$ mbar) then sealed in glass ampoules for storage prior to the NMR measurements. As shown in Figure 1, **1** is the activated cation exchanged Na/NH_4-Y zeolite (CBV300), where 80% of Na^+ are replaced by NH_4^+. Activation decomposes NH_4^+ into NH_3 and H^+, leading to protonated zeolite. **2** is the activated form of NH_4-USY (CBV500), obtained from Na/NH_4-Y by a first steaming step, followed by full NH_4^+ cation exchange. H-USY (CBV600) is then prepared by another steaming step and leads to **3** after dehydration. The final zeolite sample H-USY (CBV712) has been acidleached, as evidenced by its much lower Al content (Table S1). **4** corresponds to its activated form. All the samples were characterized by PXRD, X-Ray Fluorescence (XRF) and N_2 physisorption as reported in the Supporting Information.

2.2. Solid-State NMR Spectroscopy

The solid-state NMR sample rotors were packed in a glovebox with argon atmosphere. All the ^1H single-resonance experiments were performed at 18.8 T on a Bruker NEO narrow-bore spectrometer equipped with a 1.3 mm $^1H/^{13}C/^{15}N$ triple-resonance probe. The ^1H-^{27}Al double-resonance experiments were carried out at 13.5 T on a Bruker NEO wide-bore spectrometer equipped with a 1.3 mm ^1H/X double-resonance probe. In order to prevent the sample from absorbing moisture, a new sample rotor was packed for each experimental session and ultra-dry nitrogen gas (>99%) was used for MAS and frame-cooling. Prior to acquiring spectra, the NMR spectrometer was systematically rechecked and recalibrated, including the magic angle, the shims, the sample temperature and the chemical shift reference, to prevent any potential drift caused by instrumentation.

The quantitative 1D ^1H MAS experiments were performed with a MAS rate of 60 kHz. Before these experiments, the proton spin-lattice relaxation time constant, $T_1(^1H)$, for each resolved peak in each sample was measured by performing ^1H saturation-recovery experiments. The recycle delay (60 s) for the quantitative 1D ^1H MAS experiment was set to be larger than five times the longest $T_1(^1H)$. The probe background was removed by subtracting the spectrum of the empty rotor recorded under the same experimental conditions from each sample spectrum. For the experiment on the empty rotor, the probe tuning was checked, which was very similar to that of the packed rotor. The sample masses were recorded so that the absolute spectral intensities can be compared between different samples. 2D ^1H DQ-SQ correlation spectra were measured by using the Back-to-Back (BaBa) pulse sequence[58] with a MAS rate of 60 kHz. The broadband version BaBa pulse sequence[58] was used for TQ-SQ and 4Q-SQ correlation experiments of **4** for its improved efficiency and robustness. 2D ^1H-^{27}Al heteronuclear correlation spectra were obtained by using D-HMQC pulse sequence[59] with MAS rate of 50 kHz. The chemical shift axis of ^1H and ^{27}Al were calibrated indirectly by measuring the ^{13}C signals of adamantane and calculating the reference frequencies based on the IUPAC suggestions.[60,61] The spectral processing and deconvolution analysis of the quantitative 1D ^1H MAS spectra were all performed using TopSpin (version 4.3.0).

2.3. In Situ FTIR Spectroscopy

A self-supported wafer (1.6 cm in diameter) was activated in situ at 450 °C in a homemade IR cell attached to a dynamic vacuum system ($<10^{-5}$ mbar). After 10 h at the selected activation temperature, the sample was cooled to room temperature under dynamic vacuum. FTIR measurements were carried out using a Thermo Nexus FTIR spectrometer, equipped with a DTGS detector, in the range of 4000 – 400 cm^{-1} at a spectral resolution of 4 cm^{-1} and with 32 scans in transmission mode.

The obtained spectra were analyzed, including decomposition, integration, subtraction and determination of peak positions, using Thermo software, Omnic. Absorption coefficients used for each peak contribution are derived from the methodology of Hensen et al.[62]

2.4. DFT Calculations

Periodic DFT calculations were performed using the Vienna Ab Initio Simulation Package (VASP) code.[63,64] The Perdew, Burke and Ernzerhof (PBE) exchange and correlation functional[65] was employed, with the projected augmented wave (PAW) method[66] to describe core-electron interactions. Calculations were performed at the gamma-point with an energy cutoff of 400 eV, except for lattice optimizations, performed with an energy cutoff of 800 eV. Corrections on dispersion interactions are integrated via the D2 method of Grimme.[67] The convergence criterion for the self-consistent cycle was chosen equal or inferior to 10^{-6} eV. Geometry optimization calculations were considered converged when the force on each atom was less than 0.02 eV/Å. For non-symmetric surface slabs, a dipolar correction was added to remove unphysical interactions between vertical periodic images of the surface slabs.

Proton chemical shift tensors were calculated using the linear response method, using the gauge including projector augmented wave (GIPAW) formalism.[68,69] An energy cutoff of 600 eV was set, as well as a stricter self-consistent cycle convergence criterion of 10^{-8} eV. The step size for the finite difference k-space derivative was set to 0.001. The computed ^1H chemical shifts are referenced to tetramethylsilane.

We considered bulk and surface models of different Si/Al ratios, in some cases incorporating silanol nests and EFAL species, extracted from Jarrin et al.[70] Details about the construction of these cells can be found in the Supporting Information. In addition, dealumination intermediates proposed by Silaghi et al.[71,72] were reoptimized with the current settings and cell parameters. Moreover, a cell containing a framework-associated octahedral Al site was constructed in the spirit of Jin et al.[40] Two water molecules were coordinated to a framework Al atom of the bulk Si/Al = 3 cell. We also computed ^1H chemical shifts for the silica surface model of Tielens et al.[73] and amorphous silica-alumina (ASA) models (containing 3 or 5 water molecules per cell).[74] Indeed, ASA-like domains are sometimes invoked after dealumination.[75] The discussion of the results will also involve previously performed DFT calculations on γ-Al_2O_3 surface and edge models, which exhibit a variety of μ_1-, μ_2- and μ_3-Al-OH groups, with n in μ_n corresponding to the number of Al atoms bounded to the oxygen of the hydroxyl group.[76,77]

3. RESULTS AND DISCUSSION

3.1. Solid-State NMR Spectroscopy

1D ^1H NMR spectroscopy. The quantitative 1D ^1H MAS NMR spectra of **1-4** are shown in Figure 2, where the spectral intensities are normalized with respect to the most intense peak in each sample. The spectra in the absolute intensities and scaled to the sample mass are shown in Figure S1. The significant improvement of the ^{1}H spectral resolution by using very fast MAS rate (60 kHz) and high magnetic field (18.8 T) is demonstrated by Figure S2 in the Supporting Information. An unprecedented large number of resolved resonances is observed, whose positions and intensities continuously evolve during dealumination.

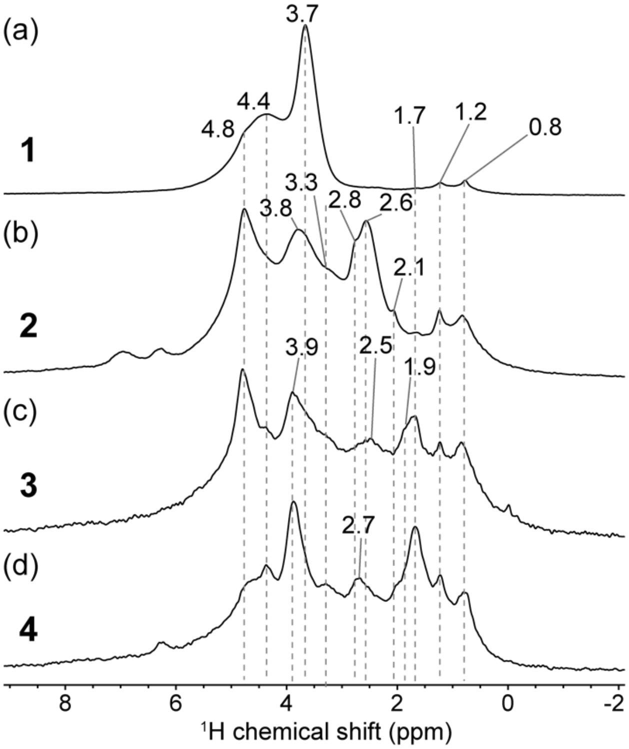

Figure 2. Quantitative ^{1}H MAS spectra of **1**-**4** (a-d). The intensities are normalized with respect to the strongest peak in each spectrum.

In the ^{1}H MAS spectrum of **1** (Figure 2a), two main resonances at 3.7 and 4.4 ppm are observed that are assigned to bridging Si-(OH)-Al hydroxyl groups pointing toward the supercage and sodalite cage, respectively.[78,79] For simplicity, they are called as supercage and sodalite Si-(OH)-Al groups, respectively, in the following. Different local environments are expected[37] and a careful inspection of the more deshielded peak reveals a shoulder peak at ca. 4.8 ppm. After the first steaming treatment and NH_4^+ exchange, in **2** the peak intensity of the bridging OH groups drastically decreases (Figure S1). This is notably the case for the resonance of Si-(OH)-Al in the supercage at 3.7 ppm (Figure 2b). Concomitantly, this resonance slightly shifts downfield at 3.8 ppm. The intensity of the resonances of the bridging OH in the sodalite cage is also strongly attenuated, the peak at 4.4 ppm being reduced by a larger extent than the one at 4.8 ppm. New resonances at 2.6 and 2.8 ppm as well as a broad shoulder peak at 3.3 ppm are observed, that are conventionally assigned to Al-OH of EFAL species.[30,56,80–85] A resonance at 2.1 ppm, often attributed to Si-OH,[28,44,47,56,85–87] is also resolved. In addition, three peaks with much lower intensity are observed at 0.8, 1.2 and 1.7, that were already present in **1**, assigned in literature to Si-OH[22,30,88–92] and/or Al-OH[22,44,56,57,76,77] groups, but with no clear consensus.

The second steaming further reduces the total spectral intensity (Figure S1). For sample **3** (Figure 2c), the peaks resonating at 4.4 and 4.8 ppm are slightly more resolved while the resonance of the Si-(OH)-Al in the supercage further shifts downfield to 3.9 ppm. The relative intensity of the resonances at 2.6 and 2.8 ppm is largely reduced, with a maximum shifting to 2.5 ppm. In contrast, the intensity for the resonance at 1.7 ppm increases significantly, and a new shoulder peak appears at ca. 1.9 ppm. The ^{1}H MAS spectrum of sample **4** obtained after acid leaching (Figure 2d and S1) is quite different. The resonance at 3.9 ppm dominates, while the signal at 4.8 ppm strongly decreases, indicating that the acid-leaching treatment impacts differently the various Si-(OH)-Al groups (see later Section 3.4). The intensities of the peaks between 2.5 and 3.3 ppm remain roughly the same. In contrast the relative as well as absolute intensity of the 1.7 ppm resonance greatly increases.

Here, we note that all NMR experiments were conducted with extreme care, and as such, a 0.1 ppm difference in peak position, e.g. between 2.5 and 2.6 ppm or 2.7 and 2.8 ppm, as shown in Figure 2, represents a measurable change. During dealumination, the relative amounts of surface species vary, altering the overall line shape and the position of local maxima. Therefore, small chemical shift variations, like those mentioned, may result from slight differences in proton chemical shift distributions.

2D ^{1}H DQ-SQ and ^{1}H{^{27}Al} D-HMQC experiments. In order to refine peak assignments, 2D ^{1}H DQ-SQ and ^{1}H{^{27}Al} D-HMQC experiments were implemented. These investigations were focused on **1** and **4**, as these two samples represent the initially non-dealuminated parent zeolite and the final catalyst produced after dealumination (i.e. after steaming and acid-leaching). Moreover, the main ^{1}H resonances observed in **2** and **3** are all present in **4**.

^{1}H{^{27}Al} D-HMQC experiment can be used to differentiate Si-OH from Si-(OH)-Al and Al-OH in zeolites. This experiment is based on through-space ^{1}H-^{27}Al heteronuclear dipolar interaction. Thus, by using short dipolar recoupling times, Si-OH groups that are not spatially close to Al atoms are filtered out. ^{1}H DQ-SQ correlation spectroscopy, making use of the through-space ^{1}H-^{1}H homonuclear dipolar interaction, provides information on whether a given species contains multiple hydroxyl groups or about spatial proximities. As it is the case for the ^{1}H{^{27}Al} D-HMQC experiment, short-range structural information is obtained when short dipolar recoupling times are used. Since these experiments require rotor-synchronization, fast MAS is advantageous, allowing the use of very short recoupling times. In this study, 600 μs and 67 μs dipolar recoupling times were used in ^{1}H{^{27}Al} D-HMQC and ^{1}H DQ-SQ experiments, respectively. As will be described below, the implementation and analysis of these 2D experiments allowed one to not only elucidate the nature of the hydroxyls with high structural details but also evidence the contributions of new species overlapping in 1D ^{1}H experiments.

As expected, the ^{1}H{^{27}Al} D-HMQC spectrum of **1** (Figure S3 and Figure 3b) is dominated by the correlations of the bridging Si-(OH)-Al species. More specifically, strong cross-peaks are observed for ^{1}H resonances in the 3.6 to 4.8 ppm range. Much weaker correlations are visible for ^{1}H at around 2.3, 2.5 and 2.7. The absence of any correlation for the 0.8, 1.2 and 1.7 ppm resonances supports their assignment to Si-OH groups.[30,93]

Figure 3c shows the SQ-dimension projection extracted from the 2D ^{1}H DQ-SQ correlation spectrum of **1**. The peaks observed in this spectrum are all mainly due to auto-correlations along the diagonal (Figure S4), i.e., they relate to species bearing multiple hydroxyl groups (≥2) or located in close proximity. The peaks at 0.8 and 1.2 ppm as well as the resonances in the 2.3-2.7 ppm range are clearly exacerbated. In the Si-(OH)-Al region, we mainly observe autocorrelations for protons at 3.6 and 4.8 ppm. The intensity of the 4.8 ppm peak associated with Si-(OH)-Al in the sodalite cage is much stronger than the 3.6 ppm resonance of the Si-(OH)-Al in the supercage, suggesting that these bridging hydroxyls are more clustered in the former cage. This is reasonable as the sodalite cage is of smaller size, i.e., favors spatial proximity. Weak off-diagonal cross-peaks are also observed between supercage and sodalite Si-(OH)-Al (Figure S4), reflecting a spatial proximity between those protons.

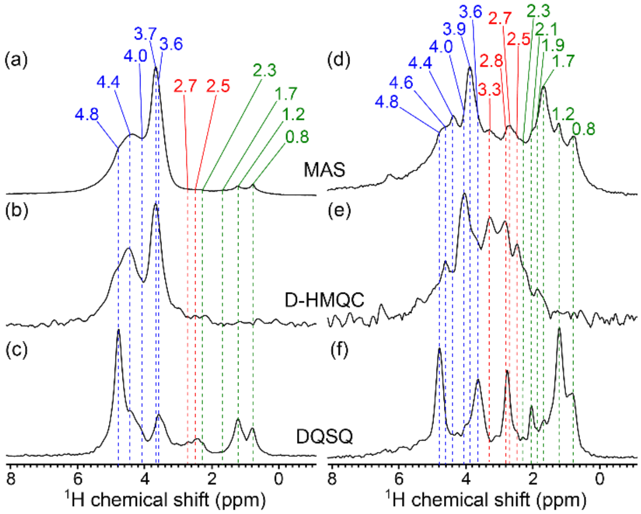

Figure 3. 1D ^{1}H MAS spectra and projections along the ^{1}H direct dimension of 2D ^{1}H{^{27}Al} D-HMQC and ^{1}H DQ-SQ correlation spectra for **1** (a, b and c) and **4** (d, e and f), respectively. Blue, red and green colors are highlighting peaks in the chemical shift range ultimately assigned to Si-(OH)-Al, Al-OH and Si-OH protons, respectively (see Table 1).

For **4**, the projection extracted from the 2D ^{1}H{^{27}Al} D-HMQC spectrum (Figure 3e) shows that all the peaks related to the different Si-(OH)-Al groups in the 3.6 to 4.8 ppm range clearly correlate with Al atoms. However, for the supercage protons, a resonance at 4.0 ppm now dominates the spectrum while the most intense signal among the sodalite Si-(OH)-Al is at 4.6 ppm. A relatively larger amount of EFAL species is expected to be present in **4** than in **1**; indeed, strong ^{27}Al correlations are observed with ^{1}H resonances at 2.5, 2.7-2.8 and 3.3 ppm (Figure 3e). Importantly, the 2D spectrum (Figure S5) shows that the ^{27}Al linewidths of these three correlation peaks are similar and noticeably smaller than those corresponding to the bridging OH between 3.6 and 4.8 ppm, meaning that ^{27}Al nuclei in these species have reduced quadrupolar couplings than those in Si-(OH)-Al groups. This observation corroborates their assignment to Al-OH in EFAL species,[82] considering that they may have multiple OH groups and/or interactions with oxygens from H_2O molecules, framework, Si-(OH)-Al, Si-OH or from other EFAL species. In Figure 3e the 2.3 ppm peak is observed as a shoulder of the 2.5 ppm peak. Weak correlation with ^{1}H at 1.9 ppm is also seen, implying that the corresponding OH groups are close to Al atoms. The absence of any correlations in **4** with protons at 0.8, 1.2 and 1.7 ppm indicates that these three types of groups are far away from any Al atom, which confirms their assignments to Si-OH groups.

As shown in the SQ-dimension projection (Figure 3f) extracted from the 2D ^{1}H DQ-SQ correlation spectrum (Figure S7) of **4**, strong auto-correlations are observed for only six ^{1}H resonances, at 0.8, 1.2, 2.1, 2.8, 3.6 and 4.8 ppm. We conclude that in the Si-(OH)-Al region the 3.6 and 4.8 ppm peaks correspond to spatially proximate (or clustered) Si-(OH)-Al groups pointing toward the supercages and sodalite cages, respectively, whereas the other belong to isolated Si-(OH)-Al. Among the three ^{1}H peaks assigned to Al-OH resonating at 2.5, 2.7-2.8 and 3.3 ppm, only the 2.7-2.8 ppm peak corresponds to species having multiple hydroxyl group protons (≥2) and/or in spatial proximity, the other two peaks corresponding to species bearing isolated hydroxyl groups. The now resolved 2.1 ppm resonance as well as the 0.8 and 1.2 ppm peaks correspond to sites having multiple hydroxyl groups (≥2) or site with Si-OH groups in spatial proximity, while the other three peaks resonating at 1.7, 1.9 and 2.3 ppm are related to isolated Si-OH.

In agreement with previous studies, cross-correlations are observed between supercage or sodalite Si-(OH)-Al groups and Al-OH groups (Figure S8). 2D ^{1}H DQ-SQ correlation spectra were also acquired on **2** and **3** (Figures S11 and S12), showing that the same set of auto-correlations are observed as in **4**, although in different intensity ratios. As a much larger amount of Al-OH groups are present in **2**, the cross-peaks mentioned in last paragraph between various Si-(OH)-Al and Al-OH groups are all very clearly detected in this sample.

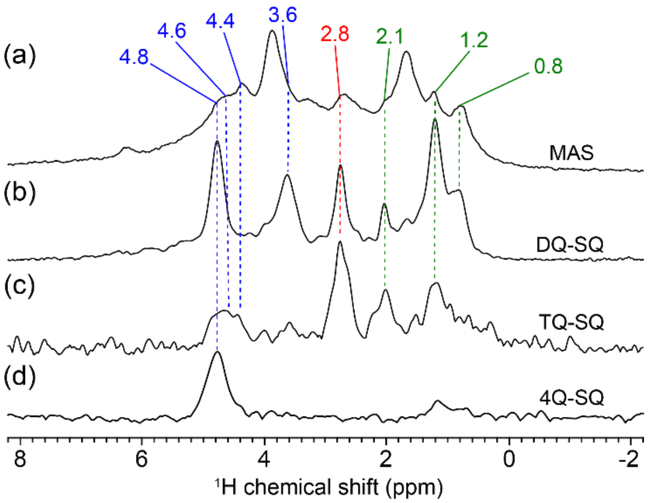

Figure 4. Comparison of the ^{1}H MAS spectrum (a) and the SQ-dimension projections extracted from the 2D ^{1}H DQ-SQ (b), TQ-SQ (c) and 4Q-SQ (d) correlation spectra of **4**.

2D ^{1}H TQ-SQ and 4Q-SQ experiments. In order to further probe the number of ^{1}H contributing to the six diagonal peaks observed in ^{1}H DQ-SQ correlation spectrum of 4 (Figure 3f), 2D ^{1}H TQ-SQ and 4Q-SQ correlation experiments were performed (Figures S9 and S10). With the same consideration as for DQ-SQ correlation experiment, short dipolar recoupling time was used to excite TQ or 4Q coherences. With these experimental conditions, mainly auto-correlation signals on the diagonal are detected in both experiments. Therefore, projections on the SQ dimension extracted from these two 2D spectra capture the essential information of the spin systems. Strong peaks are observed at 1.2, 2.1, 2.8 and 4.8 ppm in the TQ-SQ projection (Figure 4c), while resonances only appear at 1.2 and 4.8 ppm in the 4Q-SQ projection (Figure 4d). The 1D single pulse spectrum as well as the DQ-SQ projection are shown for comparison (Figure 4a and b respectively).

First, these results indicate that ^{1}H peaks at 2.1 and 2.8 ppm correspond to species having three spatially proximate protons in their structures, or four, according to the quantum mechanical selection rules for the excitation of MQ coherences that exclude the possibility of generating 4Q in a four-spin system.[94] Note that these two peaks correlate off diagonal in the 2D ^{1}H DQ-SQ correlation spectrum (Figure S7), indicating that they correspond to species in close proximity. In contrast, the 4.8 ppm peak corresponds to more than four spatially proximate (or clustered) sodalite Si-(OH)-Al. 4Q coherences are also detected at 1.2 ppm, although with a much weaker intensity, meaning that this peak mainly corresponds to 3 spatially proximate Si-OH.

3.2. DFT Calculations

The models included in the computational study (Section 2.4) encompass diverse structures in various environments. Figures 5a-h summarize the main classes of surface sites discussed here (all of them are depicted in Figure S13, and a selection of sites is depicted in Figure 6). Bridging hydroxyl groups, Si-(OH)-Al (Figure 5a, Figure 6a and c), are located both in the bulk and at the external surfaces, the latter being also representative of local environments found in the surface of mesopores formed during dealumination. Silanols (Figure 5b and 6b to f), Si-OH, are expected to be present at the framework defects, the external and mesoporous surfaces, in amorphous silica- or silica-alumina-like domains that may form through the thermal and chemical treatments. Some of the silanols exhibit aluminum as second neighbors (Figure 5c, Figure 6b, c, e) and are called silanol-Al.[31,95,96] Al-H_2O sites close to silanols (Figure 5d, Figure 6b, d and e) are expected to be present at bulk defects and external surfaces. Al-OH close to bridging OH group (Figure 5e, Figure 6c) were also modelled as well as mononuclear EFAL (Figure 5f). Some of these Al containing species interact with the framework via remaining Si-O-Al bonds leading to framework-associated defect sites (Figure 6f).[97] They exhibit μ_1-Al-OH groups, as well as Al-H_2O species. We chose not to explicitly simulate polynuclear EFAL species, even though their existence has been proposed,[98] given the vast number of potential local configurations when considering both bulk and surface sites. However, we will leverage the knowledge previously reported on ^{1}H chemical shifts for surface and edge sites of γ-Al_2O_3.[76,77] We finally modelled pseudo-bridging silanols (PBS), either PBS-Al (Figure 5g) or PBS-Si (Figure 5h) found on amorphous silica-alumina models.[74,95,99]

Computed ^{1}H NMR chemical shifts are categorized into different groups in Figure 5i. The chemical shifts of protons being hydrogen-bond (H-bond) donors are not reported as they display a dramatic downfield shift towards values around 10 ppm, which are not observed (or resolved) in experiments. Thus, we only report the chemical shifts of protons belonging to non-H-bonded OH groups and H-bond acceptors (i.e. involved in H-bond through their oxygen atom). Table S2 presents the median ^{1}H chemical shift values computed for the various classes of hydroxyl groups. Although the computed ^{1}H chemical shift distributions of the bridging hydroxyl protons in supercages and sodalite cages overlap, there is a clear shift towards higher values for the sodalite cage. This observation aligns with the findings from a previous computational study.[100] In the present work, the computed resonance frequencies of the ^{1}H lines of bridging OH groups are shifted by about 0.5 ppm with respect to the experimental data.

The median signal computed for silanol-Al appears 0.3 ppm higher than that of other Si-OH groups. This aligns very well with the experimental NMR data that identify Si-OH groups nearby Al atoms in the 1.9-2.3 ppm range and others below 1.7 ppm. However, this trend is not reproduced for H-bond acceptor Si-OH and silanol-Al. Overall, signals corresponding to Si-OH and silanol-Al overlap significantly (Figure 5i).

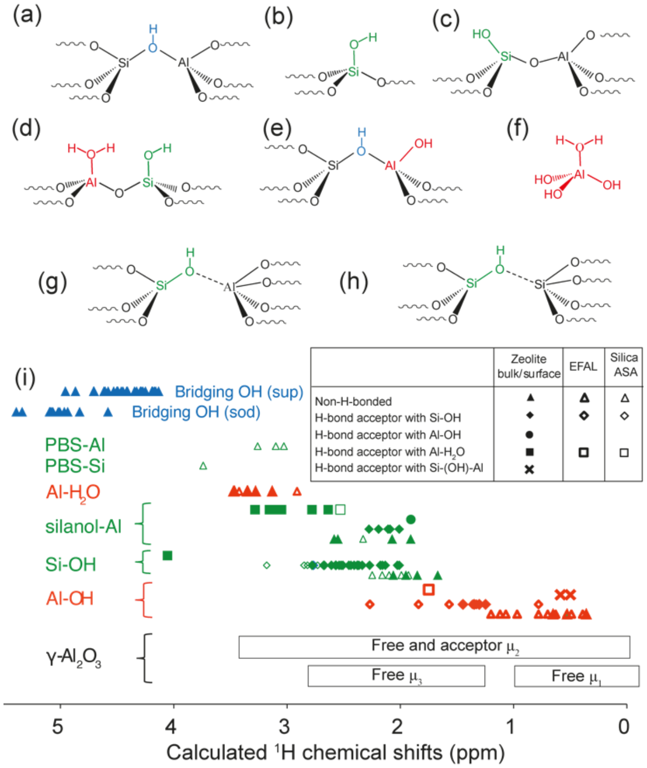

Figure 5. Various environments of hydroxyl groups computed by DFT and discussed in the present work: (a) Bridging Si-(OH)-Al group, (b) non-hydrogen bonded silanol, (c) non-hydrogen bonded silanol-Al, (d) water molecule adsorbed on Al close to a silanol, (e) μ_1-Al-OH close to a bridging OH group, (f) mononuclear $[Al(OH)_3(H_2O)]$ EFAL, (g) pseudo-bridging silanol (PBS-Al) and (h) pseudo-bridging silanol (PBS-Si). (i) ^1H chemical shifts from DFT calculations. Previous assignments for γ-Al_2O_3 are also recalled.

We note that the lowest chemical shift computed here for a Si-OH group is 1.7 ppm, whereas experimental signals as low as 1.2 and 0.8 ppm are observed. Silanols from silica and ASA (including PBS-Al and PBS-Si at 3.1 and 3.7 ppm, respectively) are mostly computed above 2 ppm, similar to zeolite surfaces. Thus, the models that we have developed so far are insufficient to explain the lowest experimentally observed chemical shifts of Si-OH groups. To account for these low chemical shifts, different surface models remain to be constructed, opening perspectives for future DFT studies that are beyond the scope of this work.

Concerning the μ_1-Al-OH groups, two distinct distributions appear, one with a median chemical shift value of 1.4 ppm corresponding to H-bond acceptors with Si-OH or Al-H_2O, and the other around 0.5-0.6 ppm for non-H-bonded Al-OH groups or H-bond acceptors with Si-(OH)-Al. While consistent with previous calculations made on ZSM-5,[31] it is important to note that these computed features solely reflect the spectroscopic properties of mononuclear aluminum species, including surface groups and Al-OH from EFAL species. The presence of multinuclear EFAL species, not considered here, could potentially lead to additional signals in the 0-3.5 ppm interval,[76,77] as shown by the γ-Al_2O_3 features reported in Figure 5i.

The Al-H_2O data presented here originate from sites modeled at the external surface, in the bulk with the presence of defects or for EFAL species. We find that these groups have chemical shifts centered around 3.4 ppm, which thus overlaps with the chemical shifts of silanol-Al. Some non-H-bonded Al-H_2O species (see later Figure 7) appear close to 2.8 ppm. In ZSM-5 zeolite, the ^1H chemical shift domain of Al-H_2O overlaps with both the domains of Si-OH and Si-(OH)-Al,[31] whereas in the present case of faujasite there is no overlap with Si-(OH)-Al domain.

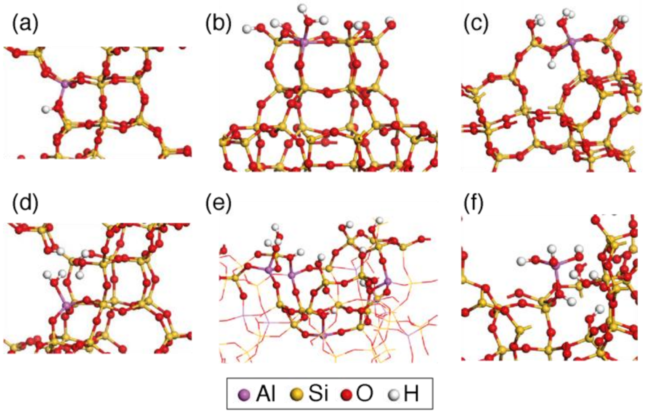

Figure 6. Some of the DFT models used for computational analysis. (a) Bulk bridging OH group at the TO1H site. (b) Al-H_2O site at the external surface of faujasite, D6R complete surface termination. (c) Al-OH and bridging OH group at the external surface, Sodalite complete surface termination. (d) Defect site at the bulk with Al-H_2O. (e) External surface model of the Y system (Si/Al = 3), Sodalite incomplete termination. (f) Dealumination intermediate starting from a bulk TO3H site, after hydrolysis of Al-O bonds by three water molecules.

It is clear from these results that the resolution of the DFT calculations in terms of spectral assignment is lower than the 0.1 ppm precision discussed experimentally. Thus, we can only comment on general trends. In fact, several computed features indicate that achieving such a level of precision for the simulated environments in presence in this work is not feasible:

i) for a given type of site, simulated in various cells, the distribution of chemical shifts is much larger than 0.1 ppm (see Figure 5i). For example, non-H-bonded μ_1-Al-OH give rise to computed shifts between 0.4 and 1.4 ppm while the computed chemical shift of non-H-bonded silanols can be found between 1.7 and 2.3 ppm.

ii) the computed chemical shifts of bridging OH groups in faujasite are found to be shifted with respect to experimental ones by about 0.5 ppm.

iii) it is known that the level of theory chosen for the theoretical study significantly impacts the results.[101] The cell size employed here, however, limits us to GGA approaches.

3.3. Assignments of the ^1H Resonances from NMR Experiments and DFT Calculations

The information derived from NMR experiments and their correlations with DFT calculations are summarized in Table 1. The following section provides a detailed breakdown of the ^1H resonance assignments and the possible local structures, zone by zone:

From 0.8 to 1.7 ppm: Through $^1H\{^{27}Al\}$ D-HMQC and ^1H MQ-SQ correlation experiments, the two ^1H signals at 0.8 and 1.2 ppm are assigned to 2 and 3 spatially proximate Si-OH groups, respectively. This confirms and refines previous assignments of these peaks to Si-OH,[22,30,88,92] contradicting other studies assigning these peaks to Al-OH[44,56,57,76,77] possibly from EFAL species. DFT calculations did not reveal any Si-OH in this zone, suggesting that the relevant environments were not adequately simulated for these signals. It is worth noting that, experimentally, similar signals have been reported in the case of silica[89,90,102] and ASA.[93,103,104] Although the computed ^1H chemical shifts of non-H-bonded μ_1-Al-OH groups fall within this zone, the absence of ^1H-^{27}Al correlation signal in this range in $^1H\{^{27}Al\}$ D-HMQC spectra indicates that they are not present. The absence of ^1H signals for edge-like sites as simulated on γ-Al_2O_3 edge models[76,77] suggests that γ-Al_2O_3-like domains are not formed after steaming. Alternatively, μ_1-Al-OH groups could potentially be formed at the external surface. Their absence aligns with DFT calculations indicating their lower stability compared to Al-H_2O groups,[70] the spectral feature of the latter appearing at higher chemical shifts (see below). As mentioned above, the 1.7 ppm resonance corresponds to isolated Si-OH groups.

From 1.9 to 3.4 ppm: $^1H\{^{27}Al\}$ D-HMQC spectra reveal that the 1.9-3.4 ppm range encompasses the presence of Al-OH groups or Si-OH groups in spatial proximity to Al. Signals falling between 1.9 and 2.3 ppm manifest in the $^1H\{^{27}Al\}$ D-HMQC spectra with significantly lower intensity compared to the 2.4–3.4 ppm signals. Consequently, the former peaks are assigned to Si-OH groups in spatial proximity to Al, while the higher chemical shift zone is attributed to Al-OH. The fact that silanol-Al would appear at higher chemical shift than Si-OH far away from Al is compatible with DFT calculations made on non-H-bonded silanols (Figure 5i). Second, in light of the DFT calculations in previous studies,[76,77] and in agreement with previous experimental data,[30,56,82,83,86] μ_2- and μ_3-Al-OH, i.e., hydroxyls belonging to multinuclear EFAL species, are expected to also yield signals in the 1.9-2.6 ppm range. Therefore, their presence in small quantities cannot be ruled out.

Most of the above-mentioned OH groups are isolated, with the exception of two ^1H signals at 2.1 and 2.7-2.8 ppm. These two signals are detected in the ^1H DQ- and TQ-SQ spectrum, while being absent in the 4Q-SQ spectrum (Figure 4), indicating a cluster of 3 or 4 protons (at most). In addition, the 2.7-2.8 ppm peak corresponds to OH groups in proximity to Al (Figure 3). Several scenarios are compatible with these observations, listed in Table 1. The 2.7-2.8 ppm signal may involve Al atoms at the external surface, framework-associated sites, or mono- or multi-nuclear EFAL species. Environments with Al-H_2O species provide 2 adjacent protons and are good candidates. Among simulated Al-H_2O species, those at the external surface result in computed chemical shifts between 3.1 and 3.5 ppm (which does not exclude a correspondence with the 2.8 ppm experimental observation). However, two bulk-like environments, illustrated in Figure 7, are computed close to 2.8 ppm. One model involves a proton from framework-associated $Al(H_2O)_2$ species resonating at 2.9 ppm, and the other model has a proton from an extra-framework $Al(OH)_3(H_2O)$ connected to a silanol nest, calculated at 2.7 ppm. However, the latter species would generate a signal in the 4Q-SQ spectrum, which is not observed, suggesting that a more accurate assignment corresponds to $Al(OH)_{0/1/2}(H_2O)_{2/1/1}$ species.

Table 1. Summary of the assignments derived from NMR experiments and DFT calculations.

$\delta(^1H)$ (ppm)	$^1H\{^{27}Al\}$ D-HMQC spectra (a)	^1H DQ-SQ spectra (a)	^1H TQ-SQ spectra (a)	^1H 4Q-SQ spectra (a)	DFT calc. (b)	Assignment (c)	IR band (cm^{-1})
0.8	✕	✓	✕	✕	✕	2 spatially proximate Si-OH	n.d. (c)
1.2	✕	✓	✓	⊘ (d)	✕	3 spatially proximate Si-OH	n.d.
1.7	✕	⊘	✕	✕	✓	isolated Si-OH (e)	3745
1.9	✓	⊘	✕	✕	✓	isolated Si-OH close to Al containing species (or possibly **μ_2- and μ_3**-Al-OH)	3740
2.1	✓	✓	✓	✕	✓	3 or 4 spatially proximate Si-OH groups close to Al (or possibly **μ_2- and μ_3**-Al-OH)	n.d.
2.3	✓	⊘	✕	✕	✓	isolated Si-OH close to Al containing species (or possibly **μ_2- and μ_3**-Al-OH)	3720

2.5-2.6	✓	⦸	✕	✕	✓	isolated μ_2- and μ_3-Al-OH involving multinuclear EFALs	3696
2.7-2.8	✓	✓	✓	✕	✓	mononuclear **external surface, framework-associated** and $Al(OH)_{0/1/2}(H_2O)_{2/1/1}$ **EFAL** species, multinuclear/clustered mononuclear EFAL species with fewer hydroxyl groups on each Al atom or **silanol-Al as H-bond acceptor with Al-H_2O**	3696
3.3	✓	⦸	✕	✕	✓	isolated Al-OH, mainly μ_2-Al-OH involving multinuclear EFALs or **possibly isolated PBS-Al of ASA zones**	3667
3.6	✓	✓	✕	✕	✕	2 spatially proximate Si-(OH)-Al pointing toward the supercages	3642 (HF")
3.7, 3.8, 3.9-4.0	✓	⦸	✕	✕	✓	isolated Si-(OH)-Al pointing toward the supercages	3642 (HF"), 3628 (HF), 3601 (HF')
4.4, 4.6	✓	⦸	✕	✕	✓	isolated Si-(OH)-Al pointing toward the sodalite cages	3565 (LF"), 3547 (LF)
4.8	✓	✓	✓	✓	✕	>4 spatially proximate Si-(OH)-Al groups pointing toward the sodalite cages	3525 (LF')

(a) These columns indicate resonances that are observed (✓) and resolved in 2D $^1H\{^{27}Al\}$ D-HMQC spectra, 2D ^1H DQ-SQ spectra, 2D ^1H TQ-SQ spectra or 2D ^1H 4Q-SQ spectra. A cross (✕) means that the resonance is not observed. (b) Environments described (✓) by DFT calculations. A cross (✕) means that no such species have been described by the models proposed herein. (c) Information specifically obtained from DFT appears in bold. (c) n.d. means not detected. (d) ⦸ denotes no or very weak auto-correlation signal corresponding to isolated OH group. (e) Isolated Si-OH refer to silanols not proximate to any other silanols (as clearly established from the absence of a resonance in the DQ-filtered spectra), corresponding to a specific type of non-bridging silanols. Blue, red and green bars separate the chemical shift range mainly assigned to Si-(OH)-Al, Al-OH and Si-OH protons, respectively.

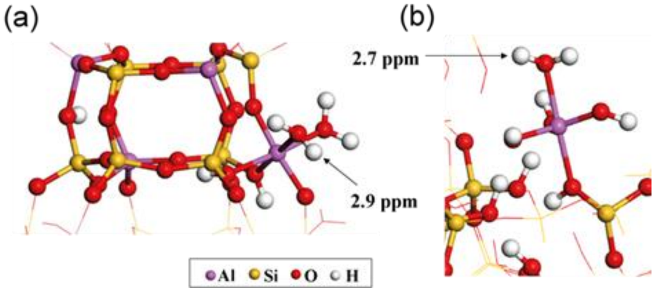

Figure 7. Two structures depicting Al-H_2O species in line with the experimental ^1H signal at 2.7-2.8 ppm: (a) framework-associated $Al(H_2O)_2$ and (b) extra-framework $Al(OH)_3(H_2O)$ connected to a silanol nest.

The signal at 3.3 ppm can be more specifically assigned to isolated μ_2-Al-OH on multinuclear EFAL species. DFT calculations suggest that some silanol-Al signals appear between 3.0 and 3.4 ppm. However, these are spatially close to other protons and act as H-bond acceptors, which is not observed experimentally. Therefore, the best correspondence between DFT and this 3.3 ppm resonance, besides μ_2-Al-OH from EFALs, is found with PBS-Al from ASA domains. To the best of our knowledge, such a detailed assignment of this spectral region has not been provided before.

From 3.6 to 4.8 ppm: We confidently assign this region to bridging OH groups based on $^1H\{^{27}Al\}$ D-HMQC experiments and DFT calculations, in line with previous knowledge.[37,79] While DFT calculations support the relative ^1H chemical shift rankings between Si-(OH)-Al groups pointing toward the supercages (3.6-4.0 ppm) and those pointing toward the sodalite cages (4.4-4.8 ppm), more subtle effects are challenging to capture through our DFT calculations, likely due to limited sampling of Al and H distributions. Thus, the comprehensive analysis presented in Table 1 primarily results from the combination of $^1H\{^{27}Al\}$ D-HMQC and ^1H MQ-SQ correlation experiments.

As only a very weak ^{1}H TQ auto-correlation signal is generated at 3.6 ppm, this peak can be assigned to mainly two spatially proximate Si-(OH)-Al groups in the supercage. In contrast, the 4.8 ppm peak corresponds to more than four spatially proximate (or clustered) Si-(OH)-Al groups pointing toward the sodalite cage, which is related to the higher probability of finding clustered Si-(OH)-Al groups in the sodalite cage. Table S3 in the Supporting Information shows the distribution of ^{1}H-^{1}H distances for the different crystallographic proton sites identified by Czjzek et al. in zeolite HNaY.[105] For O1-H located in the supercage, only 6 ^{1}H-^{1}H distances below 5 Å are calculated, while this number increases to 10 for O2-H (at the border of sodalite cage and supercage) and O3-H (in the sodalite cage), increasing the probability of 4Q-SQ correlations for sodalite cage protons.

3.4. Quantitative Analysis of Dealumination

Evolution of the bridging Si-(OH)-Al groups. The ^{1}H MAS NMR spectra of Figure S1 allow a quantitative analysis of the evolution of different OH groups during the dealumination process. The H/Na-Y zeolite **1** contains essentially bridging Si-(OH)-Al groups accounting for 83% of the total spectral intensity, 51.2 / 82.8 × 100% = 62% of them pointing toward the supercages (Table 2). According to neutron diffraction study, a majority of bridging OH groups, namely protons bond to O2 (23%) and O3 (38%), point toward the sodalite cages, while only O1 (39%) protons point toward the supercages (O4H being almost absent), in total leading to 27 and 17 protons attributed to the sodalite cages and supercages, respectively.[105] This contradiction with the experimental data, including both ours and those of others,[37] has not been pointed out before. The O2 protons at the interface between sodalite cage and supercage, can easily flip into the supercage by thermal motion. Therefore, we suggest counting these O2 protons as being part of the supercage. In that case, the percentage obtained from diffraction (61%) aligns very well with the one derived from the NMR data.

Table 2. Quantitative analysis of ^{1}H MAS spectra of 1-4.

Sample	**1**	**2**	**3**	**4**
Si-OH[a]	6.3	8.8	6.7	8.4
Al-OH[a]	2.2	12.1	3.2	3.8
Si-(OH)-Al (super)[a]	51.2	10.5	3.4	4.5
Si-(OH)-Al (sodalite)[a]	31.6	11.3	4.1	2.9
Si-(OH)-Al[a]	82.8	21.8	7.5	7.4
Total[b]	100.0	53.9	21.6	24.7
Si-(OH)-Al (super) / Total	51%	19%	16%	18%
Si-(OH)-Al (sodal.) / Total	32%	21%	19%	12%
Si-OH / Si-(OH)-Al (**1**)[c]	8%	11%	8%	10%
Al-OH / Si-(OH)-Al (**1**)[c]	3%	15%	4%	5%
Si-(OH)-Al / Si-(OH)-Al (**1**)[c]	100%	26%	9%	9%

[a] Shown in absolute intensity. The total integrated spectral intensity of **1** is scaled to 100. Resonances from 0.8 to 2.3, 2.5 to 3.3, and 3.6 to 4.0 and 4.4 to 4.8 ppm were considered for Si-OH, Al-OH, Si-(OH)-Al in supercage and Si-(OH)-Al in sodalite cage respectively (following the assignments of Table 1). [b] "Total" means the total spectral intensity of each sample. [c] Si-(OH)-Al (**1**) is the absolute intensity of Si-(OH)-Al groups in sample **1**, i.e. 82.8.

For the steamed and ion-exchanged sample **2**, we observe a sharp decrease of the intensity of the bridging OH, only 26% of the initial signal being maintained (Table 2). The decrease is larger than expected from the degree of dealumination derived from XRD; indeed, the decrease of the unit cell size indicates that the number of framework Al atoms per unit cell drops from 55 to 37 (67%). Therefore, we presume that some bridging OH groups are eliminated by ion exchange with EFAL species. While alumina-like domains are not formed, EFAL species potentially including multi-nuclear species were observed after the first steaming treatment. The decrease of the peaks ascribed to Si-(OH)-Al groups pointing toward the supercages is more pronounced than the decrease of Si-(OH)-Al groups pointing toward the sodalite cages. This indicates that either the Si-(OH)-Al groups pointing toward the supercage are the preferred sites for attack by hydrolysis, leading to dealumination, or bridging OH groups pointing toward the supercage are more prone to ion exchange with EFAL species. The former hypothesis contradicts the ranking of preferential hydrolysis initiation found by DFT,[106] suggesting that either the hypothesis is wrong or this initiation step is not the rate-limiting step, but the respective stabilities of EFAL in sodalite versus supercage could play a role.[72]

The second steaming continuously leads to a drastic intensity decrease for Si-(OH)-Al groups, only 9% of the initial amount remaining, which again exceeds the decrease expected from the degree of dealumination derived from XRD. Different from the previous treatment step, the Si-(OH)-Al groups pointing toward the two types of cages decrease by very similar amount from **2** to **3**. The acid-leaching, leading to **4**, restores partially the intensity of the supercage Si-(OH)-Al groups, likely due to the removal of EFAL species, but results in a further decrease of the intensity for the sodalite Si-(OH)-Al groups.

Evolutions of Al-OH and Si-OH groups. The dealumination process generates a complex mixture of defects and EFAL species. In the steamed and ion-exchanged zeolite **2**, several resonances in the 2.5 to 3.3 ppm range were assigned to mono- and multi-nuclear EFAL species (or framework-associated Al in the bulk and on the external surface), created by the dealumination. Their intensity corresponds to 15 % of the total Si-(OH)-Al intensity of the parent zeolite sample **1** (Table 2). Considering that the degree of dealumination is 33% based on the framework Al content deduced from XRD, we estimate that the upper-limit for the average ratio of

OH/H_2O groups coordinated/bonded to EFAL is about 0.5 H per Al atom from EFAL. After the second steaming, in **3** the overall intensity of EFAL resonances strongly decreases (Table 2), presumably because the second thermal treatment leads to a clustering of EFAL species, making them less hydroxylated. The acid-leaching restores part of the intensity of these signals. Although the acid-leaching overall removes EFAL species, the remaining ones are, therefore, again more strongly hydrated/hydroxylated.

Concerning the Si-OH groups, one might expect dealumination to create silanol nests, i.e. clustered Si-OH groups. However, we observe the appearance of the isolated silanols at 1.7 ppm after the second steaming treatment in **3**, that further increase upon acid leaching. The computed chemical shifts for silanol nests are all superior to 4 ppm, due to a dense H-bond network within the nest, and we do not expect to see a well-defined signal for such silanols. Thus, we suggest that they escape detection.

3.5. Linking ^{1}H NMR and IR Spectroscopy

IR spectroscopy is a conventional technique for investigating hydroxyl groups in zeolites, since it is highly sensitive to the OH response.[35,80,107–114] A lot of efforts have been devoted to assign the complex OH stretching vibrational spectra of USY zeolites.[107,109,115–121] However, ambiguities remain as only a few specific samples were analyzed in detail. In this final section, we demonstrate that the analyses discussed above allow improving the assignment of IR spectra obtained from the four zeolite samples.

Figure 8a shows the IR spectra of **1-4**. The bridging hydroxyl groups are easily identified for **1** by the two distinct regions: the high frequency region caused by Si-(OH)-Al groups pointing toward the supercage and vibrating at 3642 cm^{-1} (HF”) and the low frequency region due to Si-(OH)-Al groups pointing toward the sodalite cage and vibrating at 3547 cm^{-1} (LF).[80,107–112] Upon dealumination, new features are observed in the IR spectra of **2-4**. The bands at 3745 and 3740 cm^{-1} are conventionally assigned to isolated and weakly H-bonded Si-OH groups, respectively; an additional weak broad band is observed at around 3720 cm^{-1} assigned to internal silanol.[27] The band at 3696 cm^{-1} has been previously attributed to stable H_2O molecules on Na^+ that would remain after in situ thermal treatments.[122,123] The band at 3667 cm^{-1}, a position close to that of OH groups in pseudoboehmite,[124,125] is generally associated with OH groups from EFAL species. The appearance of the two bands at 3628 (HF) and 3601 cm^{-1} (HF’) is usually linked to structural changes in the framework upon dealumination impacting supercage Si-(OH)-Al groups. Two additional maxima at 3565 (LF”) and 3525 cm^{-1} (LF’) are observed in the low frequency region, which are associated with sodalite Si-(OH)-Al groups of perturbed environments.

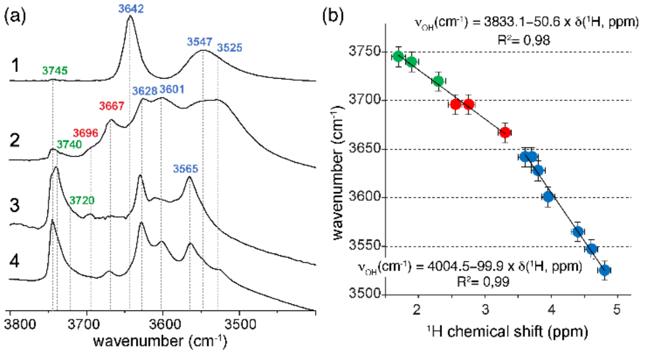

Figure 8. (a) IR spectra of **1-4**, where the intensity is normalized with respect to the strongest peak in each spectrum. (b) Correlation plot of IR wavenumbers (cm^{-1}) versus NMR ^{1}H chemical shifts (ppm). The color codes are the same as in Figure 3.

In the ^{1}H MAS NMR spectrum of **4** (Figure 2d) the 1.7 ppm peak assigned to isolated Si-OH groups dominates the silanol region (Table 1), as does the 3745 cm^{-1} band in the corresponding area of the IR spectrum (Figure 8a). According to Dib et al., non-H-bonded Si-OH groups have O-H stretching frequency in the range of 3745-3702 cm^{-1} and ^{1}H chemical shift in the range of 1.27-1.96 ppm.[92] Therefore, we associate the 3745 cm^{-1} IR band with the 1.7 ppm ^{1}H NMR peak, and assign them to isolated non-H-bonded Si-OH groups at external and mesopore surfaces. The two additional bands in this region of the IR spectra have vibration frequencies at 3740 and 3720 cm^{-1}, which is quite close to the aforementioned band at 3745 cm^{-1}. Thus, they likely correspond to species with similar environments, and we relate them to the 1.9 and 2.3 ppm ^{1}H resonances respectively, previously assigned to isolated Si-OH groups close to Al-containing species (Table 1). Travkina et al. as well as Gabrienko et al. assigned the 3740 cm^{-1} IR band to internal or defect Si-OH groups in the close vicinity to lattice imperfection or Lewis acid site (containing Al).[126,127] The two bands at 3745 and 3740 cm^{-1} have similar intensities in **3**, while the former becomes more intense in **4**, which aligns well with the trends observed in the corresponding NMR spectra for the 1.7 and 1.9 ppm resonances. This further corroborates the correlation proposed for the 1.9 ppm resonance and 3740 cm^{-1} band, and the assignment of these signals to internal or defect isolated Si-OH groups close to Al-containing species.

The 3696 cm^{-1} IR band has been attributed to H_2O molecules and therefore must correspond to the 2.7-2.8 ppm resonance, assigned from NMR and DFT calculations to EFAL with H_2O in the coordination sphere (Table 1). However, it is also possible that this IR band relates to the 2.5-2.6 ppm ^{1}H NMR peak assigned to isolated μ_2- and μ_3-Al-OH groups involving multinuclear EFAL species. The 3667 cm^{-1} IR band could be correlated with the 3.3 ppm ^{1}H peak assigned to isolated Al-OH (mainly μ_2-Al-OH groups involving multinuclear EFAL species or possibly isolated PBS-Al of ASA zones), as Travkina et al. assigned a 3675 cm^{-1} IR band observed for HY to Al-(OH)-Al groups.[126]

With this assignment, the intensity evolution of this species observed in IR (Figure S16) agrees well with that observed in NMR (Figure S1).

In the IR spectrum of **1** (Figure 8a) the 3642 cm^{-1} band dominates the region for the supercage Si-(OH)-Al groups, while in the corresponding ^1H MAS NMR spectrum (Figure 2a) the 3.7 ppm peak has the highest intensity for the same type of bridging hydroxyl groups, strongly suggesting that these two signals can be associated with each other. It should be noted that, as it is not possible to deconvolute the 3.6 and 3.7 ppm ^1H peaks, the 3642 cm^{-1} IR band may also have a contribution from the spatially proximate supercage Si-(OH)-Al groups. Upon steaming treatment, the main ^1H resonance of the supercage Si-(OH)-Al protons gradually shifts to 3.8 and 3.9-4.0 ppm, suggesting that we may correlate them with the IR bands at 3628 and 3601 cm^{-1} respectively. This assignment matches well with the intensity trends observed in the IR and NMR spectra of sample **3** and **4.**

In the low frequency region of the IR spectrum of **2** (Figure 8a), the 3525 cm^{-1} band has the highest intensity, while in the corresponding ^1H spectrum (Figure 2b) the 4.8 ppm peak dominates the region corresponding to the sodalite Si-(OH)-Al groups; in contrast, in the IR spectrum of **4** the 3565 cm^{-1} band has the highest intensity in the low frequency part and in the corresponding NMR spectrum the 4.4 ppm ^1H peak is the strongest one for the sodalite protons. Based on these observations, we tentatively correlate the 3525 and 3565 cm^{-1} IR bands with the 4.8 and 4.4 ppm ^1H resonances, respectively. The remaining 3547 cm^{-1} IR band is thus correlated with the 4.6 ppm ^1H peak.

An overall linear relationship is expected between the NMR ^1H chemical shifts and IR O-H stretching frequencies for zeolites. Figure 8b plots the NMR ^1H chemical shifts (in ppm) against the IR O-H stretching frequencies (in cm^{-1}), where the signal correlations discussed above are used. Two slopes were considered for the Si-(OH)-Al and Al-OH/Si-OH regions, respectively, each fitting the data perfectly. We note that the linear regression line for the Si-(OH)-Al data is in excellent agreement with the theoretically predicted linear relation calculated by Sierka et al.:[128]

$$\nu_{OH}\ (cm^{-1}) = 4061.7 - 113.1 \times \delta(^1H, ppm)$$

This analysis allows one to propose a new and detailed interpretation for the different IR bands of the supercage and sodalite bridging OH groups (Table 1). The correlation plot suggests that the clustered silanols assigned at 0.1, 1.2 and 2.1 ppm are not observed in the IR spectra.

Finally, a quantitative analysis of the IR spectra in the course of dealumination was performed and is reported in Table S4 and Figure S17 in the Supporting Information. While quantifying the amounts of the various OH groups from IR spectroscopy may be prone to errors due to differences in the individual absorption coefficient, a very good agreement is observed between the two techniques. This result further support not only our correlations between IR bands and ^1H NMR peaks but also the quantitative analysis results derived from the NMR data.

4. CONCLUSIONS

In this study four faujasite zeolites representing key treatment steps in industrial dealumination were investigated by high-resolution ^1H solid-state NMR spectroscopy in combination with advanced DFT calculations. The resolution of proton NMR spectra of zeolites is often limited, due to a narrow chemical shift range (typically between 0 and 5 ppm) and the presence of potentially strong homonuclear dipolar interactions. Thus, a limited number of ^1H resonances are usually resolved, preventing an in-depth spectral interpretation. Here, we addressed this issue by conducting NMR experiments at high magnetic field (18.8 T) and fast MAS rate (60 kHz), and by implementing a series of heteronuclear and homonuclear multiple-quantum filters to selectively edit subsets of resonances. A substantial number of ^1H resonances, totaling 15 peaks, could be resolved and monitored in the course of dealumination. These resonances were assigned, some unambiguously, by combining the NMR information with DFT calculations of ^1H chemical shifts. The DFT calculations were conducted on an extensive array of hydroxyl structures and environments, ranging from bulk to surfaces, also considering amorphous silica-alumina or γ-alumina domains.

Several isolated and spatially proximate bridging OH groups were identified in both the sodalite cage and the supercage. Notably, dense clusters of more than four Si-(OH)-Al were highlighted in sodalite cages. Similarly, a set of six Si-OH resonances were resolved and assigned to either isolated or clustered silanols, whether in proximity to Al atoms or not. Clusters of different sizes were again identified. While the structure of EFAL species and aluminum defects at the external surface or within the framework is still a matter of debate in dealuminated zeolites, our analysis points towards the presence of $Al(OH)_{0/1/2}(H_2O)_{2/1/1}$ species. Proximities are observed with clustered silanols, and new structural models are proposed for such species. Multinuclear or clustered mononuclear EFAL species with fewer hydroxyl groups on each Al atom are also formed, as confirmed by the comparison between the quantitative analysis of the NMR and X-ray data. Isolated Al-OH in multinuclear EFAL species or in ASA domains are also identified. In contrast, the presence of γ-alumina-like domains is excluded as free μ_1-Al-OH groups are not observed. Figures S18 to S21 show schemes illustrating the evolution of the various surface species at each stage of dealumination. The evolution of the hydroxyls groups was tracked during the dealumination process through quantitative analysis of the NMR spectra. The results indicate that either bridging hydroxyls in the supercage are more prone to dealumination than in the sodalite cage, or that protons located in the supercage are more prone to ion exchange with EFAL species. New insight into the evolution of EFAL species is also provided.

Finally, in situ IR spectra were collected on the same series of four samples. Clear correlations were established between the vibration frequencies and ^{1}H chemical shifts, that allows one to revisit and refine the assignment of faujasite IR spectra, but also provide additional information on the location of some of the hydroxyl groups.

In summary, an unprecedented large variety of hydroxyl sites were observed, identified, and monitored with a great level of structural detail during faujasite dealumination. The integrated methodology proposed here could be extended to probe the dealumination and surface structure of other zeolites. Such an advanced knowledge is crucial to rationally understand and improve the catalytic properties of these unique materials.

ASSOCIATED CONTENT

Supporting Information. Standard characterization methods, construction of the zeolite cells simulated by DFT, 2D NMR spectra and supplementary tables and figures (PDF). NMR computed data (by DFT) for this article are available at Zenodo at https://doi.org/10.5281/zenodo.13880026.

AUTHOR INFORMATION

Corresponding Authors

* Zhuoran Wang, Centre de RMN à Très Hauts Champs, Université de Lyon (CNRS/ENS Lyon/UCB Lyon 1), 69100 Villeurbanne, France, wzr8810@hotmail.com

* Gerhard Pirngruber, IFP Energies nouvelles, Rond-point de l'échangeur de Solaize, BP3, 69360 Solaize, France, gerhard.pirngruber@ifpen.fr

* Céline Chizallet, IFP Energies nouvelles, Rond-point de l'échangeur de Solaize, BP3, 69360 Solaize, France, celine.chizallet@ifpen.fr

* Anne Lesage, Centre de RMN à Très Hauts Champs, Université de Lyon (CNRS/ENS Lyon/UCB Lyon 1), 69100 Villeurbanne, France, anne.lesage@ens-lyon.fr

ACKNOWLEDGMENT

Calculations were performed using HPC resources from GENCI-CINES (Grant A0120806134) and from IFP Energies nouvelles (ENER440). This work has been supported by the Common Research laboratory CARMEN (ENS de Lyon, CNRS, IFPEN, Claude Bernard Lyon 1 University, Sorbonne University and University of Strasbourg). The partners of the project are acknowledged for valuable discussion.

REFERENCES

(1) Corma, A. State of the Art and Future Challenges of Zeolites as Catalysts. *J. Catal.* **2003**, *216* (1–2), 298–312. https://doi.org/10.1016/S0021-9517(02)00132-X.

(2) van Donk, S.; Janssen, A. H.; Bitter, J. H.; de Jong, K. P. Generation, Characterization, and Impact of Mesopores in Zeolite Catalysts. *Catal. Rev.* **2003**, *45* (2), 297–319. https://doi.org/10.1081/CR-120023908.

(3) Pérez-Ramírez, J.; Christensen, C. H.; Egeblad, K.; Christensen, C. H.; Groen, J. C. Hierarchical Zeolites: Enhanced Utilisation of Microporous Crystals in Catalysis by Advances in Materials Design. *Chem. Soc. Rev.* **2008**, *37* (11), 2530–2542. https://doi.org/10.1039/b809030k.

(4) Liang, J.; Liang, Z.; Zou, R.; Zhao, Y. Heterogeneous Catalysis in Zeolites, Mesoporous Silica, and Metal–Organic Frameworks. *Adv. Mater.* **2017**, *29* (30), 1–21. https://doi.org/10.1002/adma.201701139.

(5) Li, Y.; Yu, J. Emerging Applications of Zeolites in Catalysis, Separation and Host–Guest Assembly. *Nat. Rev. Mater.* **2021**, *6* (12), 1156–1174. https://doi.org/10.1038/s41578-021-00347-3.

(6) Chizallet, C.; Bouchy, C.; Larmier, K.; Pirngruber, G. Molecular Views on Mechanisms of Brønsted Acid-Catalyzed Reactions in Zeolites. *Chem. Rev.* **2023**, *123* (9), 6107–6196. https://doi.org/10.1021/acs.chemrev.2c00896.

(7) Corma, A. Inorganic Solid Acids and Their Use in Acid-Catalyzed Hydrocarbon Reactions. *Chem. Rev.* **1995**, *95* (3), 559–614. https://doi.org/10.1021/cr00035a006.

(8) Busca, G. Acid Catalysts in Industrial Hydrocarbon Chemistry. *Chem. Rev.* **2007**, *107* (11), 5366–5410. https://doi.org/10.1021/cr068042e.

(9) Vermeiren, W.; Gilson, J. P. Impact of Zeolites on the Petroleum and Petrochemical Industry. *Top. Catal.* **2009**, *52* (9), 1131–1161. https://doi.org/10.1007/s11244-009-9271-8.

(10) Bouchy, C.; Hastoy, G.; Guillon, E.; Martens, J. A. Fischer-Tropsch Waxes Upgrading via Hydrocracking and Selective Hydroisomerization. *Oil Gas Sci. Technol.* **2009**, *64* (1), 91–112. https://doi.org/10.2516/ogst/2008047.

(11) Bertoncini, F.; Bonduelle-Skrzypcak, A.; Francis, J.; Guillon, E., H.; Pascal, R.; Hervé, T. In Catalysis by Transition Metal Sulphides: From Molecular Theory to Industrial Applications; Toulhoat, H., Raybaud, P., Ed.; IFP publications; Technip, 2013; pp 609–677.

(12) Del Campo, P.; Martínez, C.; Corma, A. Activation and Conversion of Alkanes in the Confined Space of Zeolite-Type Materials. *Chem. Soc. Rev.* **2021**, *50* (15), 8511–8595. https://doi.org/10.1039/d0cs01459a.

(13) Ennaert, T.; Van Aelst, J.; Dijkmans, J.; De Clercq, R.; Schutyser, W.; Dusselier, M.; Verboekend, D.; Sels, B. F. Potential and Challenges of Zeolite Chemistry in the Catalytic Conversion of Biomass. *Chem. Soc. Rev.* **2016**, *45* (3), 584–611. https://doi.org/10.1039/c5cs00859j.

(14) Sudarsanam, P.; Peeters, E.; Makshina, E. V.; Parvulescu, V. I.; Sels, B. F. Advances in Porous and Nanoscale Catalysts for Viable Biomass Conversion. *Chem. Soc. Rev.* **2019**, *48* (8), 2366–2421. https://doi.org/10.1039/c8cs00452h.

(15) Bornes, C.; Santos-Vieira, I. C. M. S.; Vieira, R.; Mafra, L.; Simões, M. M. Q.; Rocha, J. Challenges and Opportunities for Zeolites in Biomass Upgrading: Impediments and Future Directions. *Catal. Today* **2023**, *419*, 114159. https://doi.org/10.1016/j.cattod.2023.114159.

(16) Martín, A. J.; Mondelli, C.; Jaydev, S. D.; Pérez-Ramírez, J. Catalytic Processing of Plastic Waste on the Rise. *Chem* **2021**, *7* (6), 1487–1533. https://doi.org/10.1016/j.chempr.2020.12.006.

(17) Dong, Z.; Chen, W.; Xu, K.; Liu, Y.; Wu, J.; Zhang, F. Understanding the Structure–Activity Relationships in Catalytic Conversion of Polyolefin Plastics by Zeolite-Based Catalysts: A Critical Review. *ACS Catal.* **2022**, *12* (24), 14882–14901. https://doi.org/10.1021/acscatal.2c04915.

(18) Marcilly, C. *Acido-Basic Catalysis: Application to Refining and Petrochemistry*; Acido-basic Catalysis: Application to Refining and Petrochemistry; Editions Technip, 2005.

(19) Silaghi, M.-C. C.; Chizallet, C.; Raybaud, P. Challenges on Molecular Aspects of Dealumination and Desilication of Zeolites. *Microporous Mesoporous Mater.* **2014**, *191*, 82–96. https://doi.org/10.1016/j.micromeso.2014.02.040.

(20) Benazzi, E.; Leite, L.; Marchal-George, N.; Toulhoat, H.; Raybaud, P. New Insights into Parameters Controlling the Selectivity in Hydrocracking Reactions. *J. Catal.* **2003**, *217* (2), 376–387. https://doi.org/10.1016/S0021-9517(03)00041-1.

(21) Fyfe, C. A.; Feng, Y.; Grondey, H.; Kokotailo, G. T.; Gies, H. One- and Two-Dimensional High-Resolution Solid-State NMR Studies of Zeolite Lattice Structures. *Chem. Rev.* **1991**, *91* (7), 1525–1543. https://doi.org/10.1021/cr00007a013.

(22) Hunger, M. Brønsted Acid Sites in Zeolites Characterized by Multinuclear Solid-State NMR Spectroscopy. *Catal. Rev.* **1997**, *39* (4), 345–393. https://doi.org/10.1080/01614949708007100.

(23) Jiang, Y.; Huang, J.; Dai, W.; Hunger, M. Solid-State Nuclear Magnetic Resonance Investigations of the Nature, Property, and Activity of Acid Sites on Solid Catalysts. *Solid State Nucl. Magn. Reson.* **2011**, *39* (3–4), 116–141. https://doi.org/10.1016/j.ssnmr.2011.03.007.

(24) Zheng, A.; Li, S.; Liu, S.-B.; Deng, F. Acidic Properties and Structure–Activity Correlations of Solid Acid Catalysts Revealed by Solid-State NMR Spectroscopy. *Acc. Chem. Res.* **2016**, *49* (4), 655–663. https://doi.org/10.1021/acs.accounts.6b00007.

(25) Paul, G.; Bisio, C.; Braschi, I.; Cossi, M.; Gatti, G.; Gianotti, E.; Marchese, L. Combined Solid-State NMR, FT-IR and Computational Studies on Layered and Porous Materials. *Chem. Soc. Rev.* **2018**, *47* (15), 5684–5739. https://doi.org/10.1039/c7cs00358g.

(26) Qi, G.; Wang, Q.; Xu, J.; Deng, F. Solid-State NMR Studies of Internuclear Correlations for Characterizing Catalytic Materials. *Chem. Soc. Rev.* **2021**, 50 (15), 8382–8399. https://doi.org/10.1039/d0cs01130d.

(27) Medeiros-Costa, I. C.; Dib, E.; Nesterenko, N.; Dath, J.-P.; Gilson, J.-P.; Mintova, S. Silanol Defect Engineering and Healing in Zeolites: Opportunities to Fine-Tune Their Properties and Performances. *Chem. Soc. Rev.* **2021**, 50 (19), 11156–11179. https://doi.org/10.1039/D1CS00395J.

(28) Omegna, A.; Vasic, M.; Van Bokhoven, J. A.; Pirngruber, G.; Prins, R. Dealumination and Realumination of Microcrystalline Zeolite Beta: An XRD, FTIR and Quantitative Multinuclear (MQ) MAS NMR Study. *Phys. Chem. Chem. Phys.* **2004**, *6* (2), 447–452. https://doi.org/10.1039/b311925d.

(29) Almutairi, S. M. T.; Mezari, B.; Filonenko, G. A.; Magusin, P. C. M. M.; Rigutto, M. S.; Pidko, E. A.; Hensen, E. J. M. Influence of Extraframework Aluminum on the Brønsted Acidity and Catalytic Reactivity of Faujasite Zeolite. *ChemCatChem* **2013**, *5* (2), 452–466. https://doi.org/10.1002/cctc.201200612.

(30) Mezari, B.; Magusin, P. C. M. M.; Almutairi, S. M. T.; Pidko, E. A.; Hensen, E. J. M. Nature of Enhanced Brønsted Acidity Induced by Extraframework Aluminum in an Ultrastabilized Faujasite Zeolite: An in Situ NMR Study. *J. Phys. Chem. C* **2021**, *125* (17), 9050–9059. https://doi.org/10.1021/acs.jpcc.1c00356.

(31) Treps, L.; Demaret, C.; Wisser, D.; Harbuzaru, B.; Méthivier, A.; Guillon, E.; Benedis, D. V.; Gomez, A.; Bruin, T. De; Rivallan, M.; Catita, L.; Lesage, A.; Chizallet, C. Spectroscopic Expression of the External Surface Sites of H-ZSM-5. *J. Phys. Chem. C* **2021**, *125* (3), 2163-2181. https://doi.org/10.1021/acs.jpcc.0c10200.

(32) Chen, K.; Zornes, A.; Nguyen, V.; Wang, B.; Gan, Z.; Crossley, S. P.; White, J. L. 17O Labeling Reveals Paired Active Sites in Zeolite Catalysts. *J. Am. Chem. Soc.* **2022**, *144* (37), 16916–16929. https://doi.org/10.1021/jacs.2c05332.

(33) Schmithorst, M. B.; Prasad, S.; Moini, A.; Chmelka, B. F. Direct Detection of Paired Aluminum Heteroatoms in Chabazite Zeolite Catalysts and Their Significance for Methanol Dehydration Reactivity. *J. Am. Chem. Soc.* **2023**, *145* (33), 18215–18220. https://doi.org/10.1021/jacs.3c05708.

(34) Ji, Y.; Chen, K.; Han, X.; Bao, X.; Hou, G. Precise Structural and Dynamical Details in Zeolites Revealed by Coupling-Edited 1 H– 17 O Double Resonance NMR Spectroscopy. *J. Am. Chem. Soc.* **2024**, *146*, 11211–11224. https://doi.org/10.1021/jacs.3c14787.

(35) Han, Y.; Larmier, K.; Rivallan, M.; Pirngruber, G. D. Generation of Mesoporosity in H–Y Zeolites by Basic or Acid/Basic Treatments: Towards a Guideline of Optimal Si/Al Ratio and Basic Reagent. *Microporous Mesoporous Mater.* **2024**, *365*, 112906. https://doi.org/10.1016/j.micromeso.2023.112906.

(36) Agostini, G.; Lamberti, C.; Palin, L.; Milanesio, M.; Danilina, N.; Xu, B.; Janousch, M.; Van Bokhoven, J. A. In Situ XAS and XRPD Parametric Rietveld Refinement to Understand Dealumination of Y Zeolite Catalyst. *J. Am. Chem. Soc.* **2010**, *132* (2), 667–678. https://doi.org/10.1021/ja907696h.

(37) Schroeder, C.; Hansen, M. R.; Koller, H. Ultrastabilization of Zeolite Y Transforms Brønsted–Brønsted Acid Pairs into Brønsted–Lewis Acid Pairs. *Angew. Chemie - Int. Ed.* **2018**, 57 (43), 14281–14285. https://doi.org/10.1002/anie.201808395.

(38) Chen, K.; Horstmeier, S.; Nguyen, V. T.; Wang, B.; Crossley, S. P.; Pham, T.; Gan, Z.; Hung, I.; White, J. L. Structure and Catalytic Characterization of a Second Framework Al(IV) Site in Zeolite Catalysts Revealed by NMR at 35.2 T. *J. Am. Chem. Soc.* **2020**, *142* (16), 7514–7523. https://doi.org/10.1021/jacs.0c00590.

(39) Chen, K.; Gan, Z.; Horstmeier, S.; White, J. L. Distribution of Aluminum Species in Zeolite Catalysts: 27 Al NMR of Framework, Partially-Coordinated Framework, and Non-Framework Moieties. *J. Am. Chem. Soc.* **2021**, *143* (17), 6669–6680. https://doi.org/10.1021/jacs.1c02361.

(40) Jin, M.; Ravi, M.; Lei, C.; Heard, C. J.; Brivio, F.; Tošner, Z.; Grajciar, L.; van Bokhoven, J. A.; Nachtigall, P. Dynamical Equilibrium between Brønsted and Lewis Sites in Zeolites: Framework-Associated Octahedral Aluminum. *Angew. Chemie - Int. Ed.* **2023**, *62* (31) e202306183. https://doi.org/10.1002/anie.202306183.

(41) Jiao, J.; Kanellopoulos, J.; Wang, W.; Ray, S. S.; Foerster, H.; Freude, D.; Hunger, M. Characterization of Framework and Extra-Framework Aluminum Species in Non-Hydrated Zeolites Y by 27Al Spin-Echo, High-Speed MAS, and MQMAS NMR Spectroscopy at B0 = 9.4 to 17.6 T. *Phys. Chem. Chem. Phys.* **2005**, *7* (17), 3221–3226. https://doi.org/10.1039/b508358c.

(42) Yu, Z.; Zheng, A.; Wang, Q.; Chen, L.; Xu, J.; Amoureux, J.; Deng, F. Insights into the Dealumination of Zeolite HY Revealed by Sensitivity-Enhanced 27 Al DQ-MAS NMR Spectroscopy at High Field. *Angew. Chemie Int. Ed.* **2010**, *49* (46), 8657–8661. https://doi.org/10.1002/anie.201004007.

(43) Shantz, D. F.; Schmedt Auf Der Günne, J.; Koller, H.; Lobo, R. F. Multiple-Quantum 1H MAS NMR Studies of Defect Sites in as-Made All- Silica ZSM-12 Zeolite. *J. Am. Chem. Soc.* **2000**, *122* (28), 6659–6663. https://doi.org/10.1021/ja000374s.

(44) Li, S.; Huang, S.-J. J.; Shen, W.; Zhang, H.; Fang, H.; Zheng, A.; Liu, S.-B. Bin; Deng, F. Probing the Spatial Proximities among Acid Sites in Dealuminated H-Y Zeolite by Solid-State NMR Spectroscopy. *J. Phys. Chem. C* **2008**, *112* (37), 14486–14494. https://doi.org/10.1021/jp803494n.

(45) Dib, E.; Grand, J.; Mintova, S.; Fernandez, C. Structure-Directing Agent Governs the Location of Silanol Defects in Zeolites. *Chem. Mater.* **2015**, *27* (22), 7577–7579. https://doi.org/10.1021/acs.chemmater.5b03668.

(46) Brunklaus, G.; Koller, H.; Zones, S. I. Defect Models of As-Made High-Silica Zeolites: Clusters of Hydrogen-Bonds and Their Interaction with the Organic Structure-Directing Agents Determined from 1 H Double and Triple Quantum NMR Spectroscopy. *Angew. Chemie Int. Ed.* **2016**, 55 (46), 14459–14463. https://doi.org/10.1002/anie.201607428.

(47) Schroeder, C.; Mück-Lichtenfeld, C.; Xu, L.; Grosso-Giordano, N. A.; Okrut, A.; Chen, C. Y.; Zones, S. I.; Katz, A.; Hansen, M. R.; Koller, H. A Stable Silanol Triad in the Zeolite Catalyst SSZ-70. *Angew. Chemie - Int. Ed.* **2020**, 59 (27), 10939–10943. https://doi.org/10.1002/anie.202001364.

(48) Derouane, E. G.; Védrine, J. C.; Ramos Pinto, R.; Borges, P. M.; Costa, L.; Lemos, M. A. N. D. A.; Lemos, F.; Ramôa Ribeiro, F. The Acidity of Zeolites: Concepts, Measurements and Relation to Catalysis: A Review on Experimental and Theoretical Methods for the Study of Zeolite Acidity. *Catal.*

Rev. - Sci. Eng. **2013**, *55* (4), 454–515. https://doi.org/10.1080/01614940.2013.822266.

(49) Bornes, C.; Fischer, M.; Amelse, J. A.; Geraldes, C. F. G. C. G. C.; Rocha, J.; Mafra, L. What Is Being Measured with P-Bearing NMR Probe Molecules Adsorbed on Zeolites? *J. Am. Chem. Soc.* **2021**, *143* (34), 13616–13623. https://doi.org/10.1021/jacs.1c05014.

(50) Sauer, J. Molecular Models in Ab Initio Studies of Solids and Surfaces: From Ionic Crystals and Semiconductors to Catalysts. *Chem. Rev.* **1989**, *89* (1), 199–255. https://doi.org/10.1021/cr00091a006.

(51) van Santen, R. A.; Kramer, G. J. Reactivity Theory of Zeolitic Bronsted Acidic Sites. *Chem. Rev.* **1995**, *95* (3), 637–660. https://doi.org/10.1021/cr00035a008.

(52) Van Speybroeck, V.; De Wispelaere, K.; Van Der Mynsbrugge, J.; Vandichel, M.; Hemelsoet, K.; Waroquier, M. First Principle Chemical Kinetics in Zeolites: The Methanol-to-Olefin Process as a Case Study. *Chem. Soc. Rev.* **2014**, *43* (21), 7326–7357. https://doi.org/10.1039/c4cs00146j.

(53) Van Speybroeck, V.; Hemelsoet, K.; Joos, L.; Waroquier, M.; Bell, R. G.; Catlow, C. R. A. Advances in Theory and Their Application within the Field of Zeolite Chemistry. *Chem. Soc. Rev.* **2015**, *44* (20), 7044–7111. https://doi.org/10.1039/c5cs00029g.

(54) Chizallet, C. Toward the Atomic Scale Simulation of Intricate Acidic Aluminosilicate Catalysts. *ACS Catal.* **2020**, *10* (10), 5579–5601. https://doi.org/10.1021/acscatal.0c01136.

(55) Chen, W.; Yi, X.; Liu, Z.; Tang, X.; Zheng, A. Carbocation Chemistry Confined in Zeolites: Spectroscopic and Theoretical Characterizations. *Chem. Soc. Rev.* **2022**, *51* (11), 4337–4385. https://doi.org/10.1039/D1CS00966D.

(56) Li, S.; Zheng, A.; Su, Y.; Zhang, H.; Chen, L.; Yang, J.; Ye, C.; Deng, F. Brønsted/Lewis Acid Synergy in Dealuminated HY Zeolite: A Combined Solid-State NMR and Theoretical Calculation Study. *J. Am. Chem. Soc.* **2007**, *129* (36), 11161–11171. https://doi.org/10.1021/ja072767y.

(57) Li, S.; Zheng, A.; Su, Y.; Fang, H.; Shen, W.; Yu, Z.; Chen, L.; Deng, F. Extra-Framework Aluminium Species in Hydrated Faujasite Zeolite as Investigated by Two-Dimensional Solid-State NMR Spectroscopy and Theoretical Calculations. *Phys. Chem. Chem. Phys.* **2010**, *12* (15), 3895. https://doi.org/10.1039/b915401a.

(58) Feike, M.; Demco, D. E.; Graf, R.; Gottwald, J.; Hafner, S.; Spiess, H. W. Broadband Multiple-Quantum NMR Spectroscopy. *J. Magn. Reson. - Ser. A* **1996**, *122* (2), 214–221. https://doi.org/10.1006/jmra.1996.0197.

(59) Hu, B.; Trébosc, J.; Amoureux, J. P. Comparison of Several Hetero-Nuclear Dipolar Recoupling NMR Methods to Be Used in MAS HMQC/HSQC. *J. Magn. Reson.* **2008**, *192* (1), 112–122. https://doi.org/10.1016/j.jmr.2008.02.004.

(60) Hoffman, R. Solid-State Chemical-Shift Referencing with Adamantane. *J. Magn. Reson.* **2022**, *340*, 107231. https://doi.org/10.1016/j.jmr.2022.107231.

(61) Harris, R. K.; Becker, E. D.; Cabral De Menezes, S. M.; Goodfellow, R.; Granger, P. NMR Nomenclature: Nuclear Spin Properties and Conventions for Chemical Shifts (IUPAC Recommendations 2001). *Concepts Magn. Reson.* **2002**, *14* (5), 326–346. https://doi.org/10.1002/cmr.10035.

(62) Poduval, D. G.; Van Veen, J. A. R.; Rigutto, M. S.; Hensen, E. J. M. Brønsted Acid Sites of Zeolitic Strength in Amorphous Silica-Alumina. *Chem. Commun.* **2010**, *46* (20), 3466–3468. https://doi.org/10.1039/c000019a.

(63) Kresse, G.; Hafner, J. Ab Initio Molecular-Dynamics Simulation of the Liquid-Metal–Amorphous-Semiconductor Transition in Germanium. *Phys. Rev. B* **1994**, *49* (20), 14251–14269. https://doi.org/10.1103/PhysRevB.49.14251.

(64) Kresse, G.; Furthmüller, J. Efficiency of Ab-Initio Total Energy Calculations for Metals and Semiconductors Using a Plane-Wave Basis Set. *Comput. Mater. Sci.* **1996**, *6* (1), 15–50. https://doi.org/10.1016/0927-0256(96)00008-0.

(65) Perdew, J. P.; Burke, K.; Ernzerhof, M. Generalized Gradient Approximation Made Simple. *Phys. Rev. Lett.* **1996**, *77* (18), 3865–3868. https://doi.org/10.1103/PhysRevLett.77.3865.

(66) Kresse, G.; Joubert, D. From Ultrasoft Pseudopotentials to the Projector Augmented-Wave Method. *Phys. Rev. B* **1999**, *59* (3), 1758–1775. https://doi.org/10.1103/PhysRevB.59.1758.

(67) Grimme, S. Semiempirical GGA-Type Density Functional Constructed with a Long-Range Dispersion Correction. *J. Comput. Chem.* **2006**, *27* (15), 1787–1799. https://doi.org/10.1002/jcc.20495.

(68) Pickard, C. J.; Mauri, F. All-Electron Magnetic Response with Pseudopotentials: NMR Chemical Shifts. *Phys. Rev. B* **2001**, *63* (24), 245101. https://doi.org/10.1103/PhysRevB.63.245101.

(69) Yates, J. R.; Pickard, C. J.; Mauri, F. Calculation of NMR Chemical Shifts for Extended Systems Using Ultrasoft Pseudopotentials. *Phys. Rev. B* **2007**, *76* (2), 024401. https://doi.org/10.1103/PhysRevB.76.024401.

(70) Jarrin, T.; de Bruin, T.; Chizallet, C. Stability and Acidity of Sites at the External Surface and at Point Defects of Faujasite. *ChemCatChem* **2023**, *15* (3), e202201302. https://doi.org/10.1002/cctc.202201302.

(71) Silaghi, M. C.; Chizallet, C.; Petracovschi, E.; Kerber, T.; Sauer, J.; Raybaud, P. Regioselectivity of Al-O Bond Hydrolysis during Zeolites Dealumination Unified by Brønsted-Evans-Polanyi Relationship. *ACS Catal.* **2015**, *5* (1), 11–15. https://doi.org/10.1021/cs501474u.

(72) Silaghi, M.-C.; Chizallet, C.; Sauer, J.; Raybaud, P. Dealumination Mechanisms of Zeolites and Extra-Framework Aluminum Confinement. *J. Catal.* **2016**, *339*, 242–255. https://doi.org/10.1016/j.jcat.2016.04.021.

(73) Tielens, F.; Gervais, C.; Lambert, J. F.; Mauri, F.; Costa, D. Ab Initio Study of the Hydroxylated Surface of Amorphous Silica: A Representative Model. *Chem. Mater.* **2008**, *20* (10), 3336–3344. https://doi.org/10.1021/cm8001173.

(74) Chizallet, C.; Raybaud, P. Pseudo-Bridging Silanols as Versatile Brønsted Acid Sites of Amorphous Aluminosilicate Surfaces. *Angew. Chemie Int. Ed.* **2009**, *48* (16), 2891–2893. https://doi.org/10.1002/anie.200804580.

(75) Barthomeuf, D. Amorphous Silica Alumina Debris in Zeolites and Zeolitic-Type Clusters in Amorphous Silica-Alumina Catalysts. *Zeolites* **1990**, *10* (2), 131–133. https://doi.org/10.1016/0144-2449(90)90031-L.

(76) Batista, A. T. F.; Wisser, D.; Pigeon, T.; Gajan, D.; Diehl, F.; Rivallan, M.; Catita, L.; Gay, A.-S.; Lesage, A.; Chizallet, C.; Raybaud, P. Beyond γ-Al2O3 Crystallite Surfaces: The Hidden Features of Edges Revealed by Solid-State 1H NMR and DFT Calculations. *J. Catal.* **2019**, *378*, 140–143. https://doi.org/10.1016/j.jcat.2019.08.009.

(77) Batista, A. T. F.; Pigeon, T.; Meyet, J.; Wisser, D.; Rivallan, M.; Gajan, D.; Catita, L.; Diehl, F.; Gay, A. S.; Chizallet, C.; Lesage, A.; Raybaud, P. Structure, Location, and Spatial Proximities of Hydroxyls on γ-Alumina Crystallites by High-Resolution Solid-State NMR and DFT Modeling: Why Edges Hold the Key. *ACS Catal.* **2023**, *13* (10), 6536–6548. https://doi.org/10.1021/acscatal.3c00495.

(78) Freude, D.; Hunger, M.; Pfeifer, H. Investigation of Acidic Properties of Zeolites by MAS NMR. *Zeitschrift fur Phys. Chemie* **1987**, *152* (1–2), 171–182. https://doi.org/10.1524/zpch.1987.152.Part_1_2.171.

(79) Peng, L.; Huo, H.; Liu, Y.; Grey, C. P. 17 O Magic Angle Spinning NMR Studies of Brønsted Acid Sites in Zeolites HY and HZSM-5. *J. Am. Chem. Soc.* **2007**, *129* (2), 335–346. https://doi.org/10.1021/ja064922z.

(80) Lohse, U.; Löffler, E.; Hunger, M.; Stöckner, J.; Patzelová, V. Hydroxyl Groups of the Non-Framework Aluminium Species in Dealuminated Y Zeolites. *Zeolites* **1987**, *7* (1), 11–13. https://doi.org/10.1016/0144-2449(87)90111-4.

(81) Mastikhin, V. M.; Mudrakovsky, I. L.; Nosov, A. V. 1H N M R Magic Angle Spinning (MAS) Studies of Heterogeneous Catalysis. *Prog. Nucl. Magn. Reson. Spectrosc.* **1991**, *23* (3), 259–299. https://doi.org/10.1016/0079-6565(91)80006-N.

(82) Jiao, J.; Altwasser, S.; Wang, W.; Weitkamp, J.; Hunger, M. State of Aluminum in Dealuminated, Nonhydrated Zeolites Y Investigated by Multinuclear Solid-State NMR Spectroscopy. *J. Phys. Chem. B* **2004**, *108* (38), 14305–14310. https://doi.org/10.1021/jp040081b.

(83) Huang, J.; Jiang, Y.; Marthala, V. R. R. R.; Thomas, B.; Romanova, E.; Hunger, M. Characterization and Acidic Properties of Aluminum-Exchanged Zeolites X and Y. *J. Phys. Chem. C* **2008**, *112* (10), 3811–3818. https://doi.org/10.1021/jp7103616.

(84) Hunger, M.; Freude, D.; Pfeifer, H. 1H MAS Studies of Acid Sites in ZSM-5 Type Zeolites. *Catal. Today* **1988**, *3* (5), 507–512. https://doi.org/10.1016/0920-5861(88)87035-4.

(85) Deng, F.; Yue, Y.; Ye, C. 1H/27Al TRAPDOR NMR Studies on Aluminum Species in Dealuminated Zeolites. *Solid State Nucl. Magn. Reson.* **1998**, *10* (3), 151–160. https://doi.org/10.1016/S0926-2040(97)00028-3.

(86) Hunger, M.; Ernst, S.; Steuernagel, S.; Weitkamp, J. High-Field 1H MAS NMR Investigations of Acidic and Non-Acidic Hydroxyl Groups in Zeolites H-Beta, H-ZSM-5, H-ZSM-58 and H-MCM-22. *Microporous Mater.* **1996**, *6* (5–6), 349–353. https://doi.org/10.1016/0927-6513(96)00043-0.

(87) Nesterenko, N. S.; Thibault-Starzyk, F.; Montouillout, V.; Yuschenko, V. V.; Fernandez, C.; Gilson, J. P.; Fajula, F.; Ivanova, I. I. Accessibility of the Acid Sites in Dealuminated Small-Port Mordenites Studied by FTIR of Co-Adsorbed Alkylpyridines and CO. *Microporous Mesoporous Mater.* **2004**, *71* (1–3), 157–166. https://doi.org/10.1016/j.micromeso.2004.03.028.

(88) Grey, C. P.; Vega, A. J. Determination of the Quadrupole Coupling Constant of the Invisible Aluminum Spins in Zeolite HY with 1H/27Al TRAPDOR NMR. *J. Am. Chem. Soc.* **1995**, *117* (31), 8232–8242. https://doi.org/10.1021/ja00136a022.

(89) Dorémieux-Morin, C.; Heeribout, L.; Dumousseaux, C.; Fraissard, J.; Hommel, H.; Legrand, A. P.; Doremieux-Morin, C.; Heeribout, L.; Dumousseaux, C.; Fraissard, J.; Hommel, H.; Legrand, A. P. Study of the Constitutive Superficial Water of Precipitated Amorphous Silicas Using 1 H NMR: Broad-Line at 4 K and HR MAS at 300 K. *J. Am. Chem. Soc.* **1996**, *118* (51), 13040–13045. https://doi.org/10.1021/ja962057k.

(90) Hartmeyer, G.; Marichal, C.; Lebeau, B.; Rigolet, S.; Caullet, P.; Hernandez, J. Speciation of Silanol Groups in Precipitated Silica Nanoparticles by 1H MAS NMR Spectroscopy. *J. Phys. Chem. C* **2007**, *111* (26), 9066–9071. https://doi.org/10.1021/jp071490l.

(91) Vidal-Moya, J. A.; Blasco, T.; Rey, F.; Valencia, S.; Corma, A. Characterization of LTA- and CHA- Type Zeolites by Means of Solid State NMR. In *Studies in Surface Science and Catalysis*; Elsevier B.V., 2008; Vol. 174, pp 989–992. https://doi.org/10.1016/S0167-2991(08)80056-0.

(92) Dib, E.; Costa, I. M.; Vayssilov, G. N.; Aleksandrov, H. A.; Mintova, S. Complex H-Bonded Silanol Network in Zeolites Revealed by IR and NMR Spectroscopy Combined with DFT Calculations. *J. Mater. Chem. A* **2021**, *9* (48), 27347–27352. https://doi.org/10.1039/D1TA06908J.

(93) Hensen, E. J. M.; Poduval, D. G.; Degirmenci, V.; Ligthart, D. A. J. M.; Chen, W.; Maugé, F.; Rigutto, M. S.; Veen, J. A. R. Van. Acidity Characterization of Amorphous Silica-Alumina. *J. Phys. Chem. C* **2012**, *116* (40), 21416–21429. https://doi.org/10.1021/jp309182f.

(94) Tycko, R. Selection Rules for Multiple Quantum NMR Excitation in Solids: Derivation from Time-Reversal Symmetry and Comparison with Simulations and 13C NMR Experiments. *J. Magn. Reson.* **1999**, *139* (2), 302–307. https://doi.org/10.1006/jmre.1999.1776.

(95) Chizallet, C.; Raybaud, P. Acidity of Amorphous Silica–Alumina: From Coordination Promotion of Lewis Sites to Proton Transfer. *ChemPhysChem* **2010**, *11* (1), 105–108. https://doi.org/10.1002/cphc.200900797.

(96) Leydier, F.; Chizallet, C.; Chaumonnot, A.; Digne, M.; Soyer, E.; Quoineaud, A.-A.; Costa, D.; Raybaud, P. Brønsted Acidity of Amorphous Silica–Alumina: The Molecular Rules of Proton Transfer. *J. Catal.* **2011**, *284* (2), 215–229. https://doi.org/10.1016/j.jcat.2011.08.015.

(97) Ravi, M.; Sushkevich, V. L.; van Bokhoven, J. A. Towards a Better Understanding of Lewis Acidic Aluminium in Zeolites. *Nat. Mater.* **2020**, *19* (10), 1047–1056. https://doi.org/10.1038/s41563-020-0751-3.

(98) Liu, C.; Li, G.; Hensen, E. J. M.; Pidko, E. A. Nature and Catalytic Role of Extraframework Aluminum in Faujasite Zeolite: A Theoretical Perspective. *ACS Catal.* **2015**, 5 (11), 7024–7033. https://doi.org/10.1021/acscatal.5b02268.

(99) Valla, M.; Rossini, A. J.; Caillot, M.; Chizallet, C.; Raybaud, P.; Digne, M.; Chaumonnot, A.; Lesage, A.; Emsley, L.; Van Bokhoven, J. A.; Copéret, C. Atomic Description of the Interface between Silica and Alumina in Aluminosilicates through Dynamic Nuclear Polarization Surface-Enhanced NMR Spectroscopy and First-Principles Calculations. *J. Am. Chem. Soc.* **2015**, *137* (33), 10710–10719. https://doi.org/10.1021/jacs.5b06134.

(100) Eichler, U.; Brändle, M.; Sauer, J. Predicting Absolute and Site Specific Acidities for Zeolite Catalysts by a Combined Quantum Mechanics/Interatomic Potential Function Approach. *J. Phys. Chem. B* **1997**, *101* (48), 10035–10050. https://doi.org/10.1021/jp971779a.

(101) Windeck, H.; Berger, F.; Sauer, J. Spectroscopic Signatures of Internal Hydrogen Bonds of Brønsted-Acid Sites in the Zeolite H-MFI. *Angew. Chemie - Int. Ed.* **2023**, *62* (25), e202303204. https://doi.org/10.1002/anie.202303204.

(102) Gay, I. D. A Magic-Angle Spinner for Vacuum-Sealed Samples. *J. Magn. Reson.* **1984**, *58* (3), 413–420. https://doi.org/10.1016/0022-2364(84)90145-8.

(103) Bronnimann, C. E.; Chuang, I. ssuer; Hawkins, B. L.; Maciel, G. E. Dehydration of Silica—Aluminas Monitored by High-Resolution Solid-State Proton NMR. *J. Am. Chem. Soc.* **1987**, *109* (5), 1562–1564. https://doi.org/10.1021/ja00239a043.

(104) Crépeau, G.; Montouillout, V.; Vimont, A.; Mariey, L.; Cseri, T.; Maugé, F. Nature, Structure and Strength of the Acidic Sites of Amorphous Silica Alumina: An IR and NMR Study. *J. Phys. Chem. B* **2006**, *110* (31), 15172–15185. https://doi.org/10.1021/jp062252d.

(105) Czjzek, M.; Jobic, H.; Fitch, A. N.; Vogt, T. Direct Determination of Proton Positions in D-Y and H-Y Zeolite Samples by Neutron Powder Diffraction. *J. Phys. Chem.* **1992**, *96* (4), 1535–1540. https://doi.org/10.1021/j100183a009.

(106) Jarrin, T.; de Bruin, T.; Chizallet, C. Impact of Point Defects, External Surfaces Sites, and Si/Al Ratio on Al–O Bonds Hydrolysis Kinetics at the Initiation of Faujasite Dealumination. *ACS Catal.* **2024**, *14* (3), 1639–1652. https://doi.org/10.1021/acscatal.3c05517.

(107) Jacobs, P. A.; Uytterhoeven, J. B. Assignment of the Hydroxyl Bands in the Infrared Spectra of Zeolites X and Y. Part 2. - After Different Pretreatments. *J. Chem. Soc. Faraday Trans. 1 Phys. Chem. Condens. Phases* **1973**, *69*, 373–386. https://doi.org/10.1039/F19736900373.

(108) Fritz, P. O.; Lunsford, J. H. The Effect of Sodium Poisoning on Dealuminated Y-Type Zeolites. *J. Catal.* **1989**, *118* (1), 85–98. https://doi.org/10.1016/0021-9517(89)90303-5.

(109) Khabtou, S.; Chevreau, T.; Lavalley, J. C. Quantitative Infrared Study of the Distinct Acidic Hydroxyl Groups Contained in Modified Y Zeolites. *Microporous Mater.* **1994**, *3* (1–2), 133–148. https://doi.org/10.1016/0927-6513(94)00015-8.

(110) Cairon, O.; Chevreau, T. Quantitative FTIR Studies of

Hexagonal and Cubic Faujasites by Pyridine and CO Adsorption: Numbers and Relative Acidity of the HF and LF Zeolitic Hydroxy Groups. *J. Chem. Soc. - Faraday Trans.* **1998**, *94* (2), 323–330. https://doi.org/10.1039/a703444j.

(111) Cairon, O.; Chevreau, T.; Lavalley, J. C. Brønsted Acidity of Extraframework Debris in Steamed Y Zeolites from the FTIR Study of CO Adsorption. *J. Chem. Soc. - Faraday Trans.* **1998**, *94* (19), 3039–3047. https://doi.org/10.1039/a803886d.

(112) Cairon, O. Impacts of Composition and Post-Treatment on the Brønsted Acidity of Steam-Treated Faujasite: Insights from FTIR Spectroscopy. *ChemPhysChem* **2013**, *14* (1), 244–251. https://doi.org/10.1002/cphc.201200568.

(113) Hadjiivanov, K. *Identification and Characterization of Surface Hydroxyl Groups by Infrared Spectroscopy*, 1st ed.; Elsevier Inc., 2014; Vol. 57. https://doi.org/10.1016/B978-0-12-800127-1.00002-3.

(114) Bordiga, S.; Lamberti, C.; Bonino, F.; Travert, A.; Thibault-Starzyk, F. Probing Zeolites by Vibrational Spectroscopies. *Chem. Soc. Rev.* **2015**, *44* (20), 7262–7341. https://doi.org/10.1039/c5cs00396b.

(115) Scherzer, J.; Bass, J. L. Infrared Spectra of Ultrastable Zeolites Derived from Type Y Zeolites. *J. Catal.* **1973**, *28* (1), 101–115. https://doi.org/10.1016/0021-9517(73)90184-X.

(116) Chevreau, T.; Chambellan, A.; Lavalley, J. C.; Catherine, E.; Marzin, M.; Janin, A.; Hémidy, J. F.; Khabtou, S. Amorphization Levels, Nature and Localization of the Extraframework Phases of Dealuminated Y Zeolites. *Zeolites* **1990**, *10* (4), 226–234. https://doi.org/10.1016/0144-2449(94)90133-3.

(117) Chambellan, A.; Chevreau, T.; Khabtou, S.; Marzin, M.; Lavalley, J. C. Acidic Sites of Steamed HY Zeolites, Active for Benzene Self-Alkylation and Hydrogenation. *Zeolites* **1992**, *12* (3), 306–314. https://doi.org/10.1016/S0144-2449(05)80300-8.

(118) Makarova, M. A.; Dwyer, J. FTIR Analysis of the Hydroxyl Region in US-Y Zeolites. *J. Phys. Chem.* **1993**, *97* (24), 6337–6338. https://doi.org/10.1021/j100126a004.

(119) Mariey, L.; Khabtou, S.; Marzin, M.; Lavalley, J. C.; Chambellan, A.; Chevreau, T. Acidity and Reactivity of Steamed HY Zeolites Obtained by Progressive Extraction of Extraframework Al Species. In *Zeolites: A Refined Tool for Designing Catalytic Sites*; Bonneviot, L., Kaliaguine, S. B. T.-S. in S. S. and C., Eds.; Elsevier, 1995; Vol. 97, pp 501–506. https://doi.org/https://doi.org/10.1016/S0167-2991(06)81930-0.

(120) Morin, S.; Berreghis, A.; Ayrault, P.; Gnep, N. S.; Guisnet, M. Dealumination of Zeolites Part VIII Acidity and Catalytic Properties of HEMT Zeolites Dealuminated by Steamingf. *J. Chem. Soc. - Faraday Trans.* **1997**, *93* (17), 3269–3275. https://doi.org/10.1039/a702538f.

(121) Cairon, O.; Thomas, K.; Chevreau, T. FTIR Studies of Unusual OH Groups in Steamed HNaY Zeolites: Preparation and Acid Properties. *Microporous Mesoporous Mater.* **2001**, *46* (2–3), 327–340. https://doi.org/10.1016/S1387-1811(01)00316-X.

(122) Ward, J. W. Spectroscopic Study of the Surface of Zeolite Y. II. Infrared Spectra of Structural Hydroxyl Groups and Adsorbed Water on Alkali, Alkaline Earth, and Rare Earth Ion-Exchanged Zeolites. *J. Phys. Chem.* **1968**, *72* (12), 4211–4223. https://doi.org/10.1021/j100858a046.

(123) Cairon, O.; Loustaunau, A.; Gautier, M. FTIR Studies of Unusual OH Groups in Steamed HNaY Zeolites: Influence of Na Insertion. *J. Phys. Chem. Solids* **2006**, *67* (5–6), 994–997. https://doi.org/10.1016/j.jpcs.2006.01.073.

(124) Ward, J. W. Thermal Decomposition of Ammonium Y Zeolite. *J. Catal.* **1970**, *18* (3), 348–351. https://doi.org/10.1016/0021-9517(70)90331-3.

(125) Shannon, R. D.; Gardner, K. H.; Staley, R. H.; Bergeret, G.; Gallezot, P.; Auroux, A. The Nature of the Nonframework Aluminum Species Formed during the Dehydroxylation of H-Y. *J. Phys. Chem.* **1985**, *89* (22), 4778–4788. https://doi.org/10.1021/j100268a025.

(126) Travkina, O. S.; Agliullin, M. R.; Filippova, N. A.; Khazipova, A. N.; Danilova, I. G.; Grigor'Eva, N. G.; Narender, N.; Pavlov, M. L.; Kutepov, B. I. Template-Free Synthesis of High Degree Crystallinity Zeolite y with Micro-Meso-Macroporous Structure. *RSC Adv.* **2017**, *7* (52), 32581–32590. https://doi.org/10.1039/c7ra04742h.

(127) Gabrienko, A. A.; Danilova, I. G.; Arzumanov, S. S.; Toktarev, A. V.; Freude, D.; Stepanov, A. G. Strong Acidity of Silanol Groups of Zeolite Beta: Evidence from the Studies by IR Spectroscopy of Adsorbed CO and 1H MAS NMR. *Microporous Mesoporous Mater.* **2010**, *131* (1–3), 210–216. https://doi.org/10.1016/j.micromeso.2009.12.025.

(128) Sierka, M.; Eichler, U.; Datka, J.; Sauer, J. Heterogeneity of Brønsted Acidic Sites in Faujasite Type Zeolites Due to Aluminum Content and Framework Structure. *J. Phys. Chem. B* **1998**, *102* (33), 6397–6404. https://doi.org/10.1021/jp981670i.

Table of Contents artwork